Research Article

Mineralogy, Structure, and Habitability of Carbon-Enriched Rocky Exoplanets: A Laboratory Approach

Kaustubh Hakim,[1,2,*] Rob Spaargaren,[3] Damanveer S. Grewal,[4] Arno Rohrbach,[5]
Jasper Berndt,[5] Carsten Dominik,[1] and Wim van Westrenen[2]

Abstract

Carbon-enriched rocky exoplanets have been proposed to occur around dwarf stars as well as binary stars, white dwarfs, and pulsars. However, the mineralogical make up of such planets is poorly constrained. We performed high-pressure high-temperature laboratory experiments ($P = 1$–2 GPa, $T = 1523$–1823 K) on chemical mixtures representative of C-enriched rocky exoplanets based on calculations of protoplanetary disk compositions. These *P-T* conditions correspond to the deep interiors of Pluto- to Mars-sized planets and the upper mantles of larger planets. Our results show that these exoplanets, when fully differentiated, comprise a metallic core, a silicate mantle, and a graphite layer on top of the silicate mantle. Graphite is the dominant carbon-bearing phase at the conditions of our experiments with no traces of silicon carbide or carbonates. The silicate mineralogy comprises olivine, orthopyroxene, clinopyroxene, and spinel, which is similar to the mineralogy of the mantles of carbon-poor planets such as the Earth and largely unaffected by the amount of carbon. Metals are either two immiscible iron-rich alloys (S-rich and S-poor) or a single iron-rich alloy in the Fe-C-S system with immiscibility depending on the S/Fe ratio and core pressure. We show that, for our C-enriched compositions, the minimum carbon abundance needed for C-saturation is 0.05–0.7 wt% (molar C/O $\sim$ 0.002–0.03). Fully differentiated rocky exoplanets with C/O ratios more than that needed for C-saturation would contain graphite as an additional layer on top of the silicate mantle. For a thick enough graphite layer, diamonds would form at the bottom of this layer due to high pressures. We model the interior structure of Kepler-37b and show that a mere 10 wt% graphite layer would decrease its derived mass by 7%, which suggests that future space missions that determine both radius and mass of rocky exoplanets with insignificant gaseous envelopes could provide quantitative limits on their carbon content. Future observations of rocky exoplanets with graphite-rich surfaces would show low albedos due to the low reflectance of graphite. The absence of life-bearing elements other than carbon on the surface likely makes them uninhabitable. Key Words: Carbon-rich—Rocky exoplanets—Mineralogy—High-pressure—Laboratory experiments—Habitability. Astrobiology 19, xxx–xxx.

1. Introduction

SINCE THE DISCOVERY of the first rocky exoplanet, CoRoT-7b (Léger *et al.*, 2009), more than 1000 such planets have been found. The scatter in the mass-radius diagram of rocky exoplanets reveals a great diversity in their bulk composition and interior structure (*e.g.*, Valencia *et al.*, 2006; Seager *et al.*, 2007; Wagner *et al.*, 2011; Hakim *et al.*, 2018a). Water/ices (*e.g.*, GJ 876d, Valencia *et al.*, 2007), thick at-

mospheres (*e.g.*, GJ 1132b, Southworth *et al.*, 2017), as well as carbon-bearing minerals, including graphite and silicon carbide (*e.g.*, 55 Cancri e, Madhusudhan *et al.*, 2012), have been suggested as dominant phases in these exoplanets, in addition to silicate minerals and iron alloys. Besides dwarf stars, carbon-enriched rocky exoplanets have been proposed around binary stars (*e.g.*, Whitehouse *et al.*, 2018) as well as pulsars and white dwarf stars (*e.g.*, Kuchner and Seager, 2005).

[1]Anton Pannekoek Institute for Astronomy, University of Amsterdam, Amsterdam, The Netherlands.
[2]Department of Earth Sciences, Vrije Universiteit Amsterdam, Amsterdam, The Netherlands.
[3]Department of Earth Sciences, ETH Zürich, Zürich, Switzerland.
[4]Department of Earth, Environmental and Planetary Sciences, Rice University, Houston, Texas.
[5]Institut für Mineralogie, Westfälische Wilhelms-Universität Münster, Münster, Germany.
*Current Affiliation: Center for Space and Habitability, University of Bern, Bern, Switzerland.

Although life as we know it is largely based on carbon, the Earth contains less than 0.01 wt% carbon (*e.g.*, Javoy *et al.*, 2010). This is to some extent surprising, since many weakly processed planetary building blocks in the solar system contain significant amounts of carbon in the form of organics (*e.g.*, carbonaceous chondrites, Marty *et al.*, 2013), and some larger, more evolved bodies such as the ureilite parent body contain significant amounts of refractory carbon (Nabiei *et al.*, 2018). To explain the extremely low abundance of carbon in the Earth, carbon needs to be burned (oxidized and turned into CO/CO_2) or photolyzed away (broken out of the organic compounds by energetic photons) while the solid material is still present in the form of small grains with large surface-to-mass ratio (Lee *et al.*, 2010; Anderson *et al.*, 2017).

An alternative explanation is that planetesimal-sized parent bodies need to be subjected to igneous processing to degas carbon (Hashizume and Sugiura, 1998), which is tied to the presence of radioactive elements such as ^{26}Al in the early solar nebula (Hevey and Sanders, 2006). Both these processes do not seem inevitable. Oxidation and photoprocessing may be quenched by effects of dust growth and transport in disks (Klarmann *et al.*, 2018). The presence of short-lived radioactive isotopes in significant amounts requires the fast (within a Myr) addition of the ejecta of a nearby supernova explosion or stellar wind material into the collapsing protosolar cloud, followed by rapid formation of planetesimals (Bizzarro *et al.*, 2005). It is therefore likely that the conditions needed to decarbonize solids are absent in many planet-forming systems, and that rocky planets in such systems may contain significant levels of carbon up to 10 mass percent.

Even larger carbon abundance could be obtained in systems where the carbon-to-oxygen abundance ratio is higher than in the solar system. Modeling of the protoplanetary disk chemistry for planet-hosting stars with molar photospheric C/O >0.65 (Moriarty *et al.*, 2014) and C/O >0.8 (Bond *et al.*, 2010; Carter-Bond *et al.*, 2012b) (cf. $C/O_{Sun} \sim 0.54$) suggests that carbon acts as a refractory element mainly in the form of graphite and silicon carbide in the inner regions of such disks. Delgado Mena *et al.* (2010) and Petigura and Marcy (2011) reported spectroscopic observations of stars with photospheric C/O ratios greater than unity. However, Nakajima and Sorahana (2016) and Brewer *et al.* (2016) claimed that the stars in solar neighborhood have largely solar-like C/O ratios. Although the debate over photospheric C/O ratios is not settled, the possibility of a substantial fraction of stars with C/O >0.65 cannot be excluded.

Refractory elements in protoplanetary disks are the major building blocks of rocky planets. Bond *et al.* (2010) found that the C/O ratio of the refractory material in inner disks of stars with C/O >0.8 varies from 0 to greater than 100 as a function of distance from the star. Moriarty *et al.* (2014) found that for high C/O stars, the extent of refractory carbon in the planetesimal disk increases when using a sequential condensation model instead of a simple equilibrium condensation model. Thiabaud *et al.* (2015) showed that C/O ratios of rocky planets do not necessarily show a one-to-one correlation with the stellar photospheric C/O ratios. N-body simulations by Bond *et al.* (2010) produce rocky exoplanets containing as high as 70 wt% carbon. The amount and nature of carbon-bearing minerals in carbon-enriched rocky exoplanets may directly impact geodynamical processes, carbon and water cycles, and in turn planetary habitability (Unterborn *et al.*, 2014).

During the early stages of planet formation, refractory material in protoplanetary disks condenses out from the chemical reactions between gas molecules. Coagulation of refractory material leads to the formation of pebbles, which grow into sub-Ceres-sized to Pluto-sized planetesimals and later on form planets (Johansen *et al.*, 2007; Schäfer *et al.*, 2017). Such planetesimals are large enough to undergo large-scale differentiation at high-pressure high-temperature conditions during the process of planet formation. Modeling studies such as those of Bond *et al.* (2010) and Moriarty *et al.* (2014) derive proportions of chemical compounds condensing out from gas chemistry and perform N-body simulations on planetesimals to track the likely chemical composition of resulting planets. Since the pressures in the interiors of planetesimals and planets are several orders of magnitude higher than the disk pressures, high-pressure high-temperature reactions are expected to reprocess their chemical composition and kick off large-scale differentiation processes in their interiors, which lead to metal segregation and core formation (Kruijer *et al.*, 2013). Current understanding of the mineralogy of exoplanets is based on extrapolation of the knowledge of rocky bodies in our solar system and lacks experimental evidence. There is a need to investigate the mineralogy and phase relationships between carbon-rich planetesimals and exoplanets, which have no Solar system analogues, in multicomponent systems, and high-pressure high-temperature experiments make it possible (*e.g.*, Valencia *et al.*, 2009; Nisr *et al.*, 2017).

C-enriched rocky exoplanets are speculated to contain large amounts of C-bearing minerals, including silicon carbide and graphite (*e.g.*, Bond *et al.*, 2010; Madhusudhan *et al.*, 2012). Over the past decades, several laboratory studies have investigated the mineralogy of rocky planets in C-poor Earth-like conditions, but only a few studies are applicable to conditions relevant to C-enriched exoplanetary interiors. Corgne *et al.* (2008) used a CI-chondrite-like composition to probe early planetesimal differentiation in carbon- and sulfur-enhanced environments and observed liquid metal immiscibility leading to the formation of C-rich and S-rich metals. The extent of liquid metal immiscibility has been explored in the simple Fe-C-S (*e.g.*, Dasgupta *et al.*, 2009), Fe-S-O (*e.g.*, Tsuno *et al.*, 2007), and Fe-S-Si (*e.g.*, Morard and Katsura, 2010) systems. The solubility of carbon in iron alloys (*e.g.*, Lord *et al.*, 2009; Tsuno and Dasgupta, 2015) and silicate melts (*e.g.*, Duncan *et al.*, 2017), the partitioning of carbon between silicate melt and iron alloys (*e.g.*, Chi *et al.*, 2014; Li *et al.*, 2015, 2016), and the stability of reduced versus oxidized carbon in the Earth's mantle (*e.g.*, Rohrbach and Schmidt, 2011) have also been investigated. Phase relationships have been studied in the carbon-saturated Fe-Mg-Si-C-O (FMS+CO) system with bulk compositions depleted in oxygen (Takahashi *et al.*, 2013). The study by Takahashi *et al.* (2013) covers a range of oxygen fugacities resembling highly reducing conditions; however, they did not consider the presence of S, which can be a major component in the Fe-rich cores of rocky bodies (*e.g.*, Stewart *et al.*, 2007; Rai and van Westrenen, 2013; Steenstra *et al.*, 2016). Moreover, they lack a discussion about the diversification of silicate minerals due to the absence of Al and Ca in their experiments. Finally, to our knowledge, no experimental studies have used C-enriched starting compositions calculated by modeling planet formation

chemistry around stars other than our Sun, which is key for future exoplanetary exploration.

Here we probe the mineralogy and structure of small C-enriched rocky exoplanets by performing high-pressure high-temperature laboratory experiments on chemical mixtures in the Fe-Ca-Mg-Al-Si-C-S-O (FCMAS+CSO) system, resembling the bulk compositions of C-enriched planetesimals from the models of Moriarty *et al.* (2014). In Section 2, we give our experimental and analytical methods. Phase relationships and compositions of our experimental run products are given in Section 3. The mineralogy and structure of C-enriched rocky exoplanets and their dependence on several factors are discussed in Section 4. To illustrate the application of our findings, we discuss the implications of assuming a C-enriched interior on the derived mass, future observations, and habitability of Kepler-37b, the smallest known exoplanet till date, in Section 5. Finally, we summarize our findings and conclusions in Section 6.

2. Methods

2.1. Choice of bulk compositions

To prepare starting materials for our experiments, we used relative elemental abundances of C-enriched planetesimals at 1 AU and 0.15 Myr after disk formation in the HD19994 planetary system calculated by Moriarty *et al.* (2014) for their equilibrium chemistry (EC) and sequential condensation chemistry (SC) cases. Two end-member compositions (SC and EC) were prepared by using elemental proportions given in Table 1. The C/O ratios of the SC and EC compositions are 0.35 and 1.38, respectively, about two-three orders of magnitude higher than that of the Earth, and they give an appropriate range of carbon-enriched compositions based on the calculations of Moriarty *et al.* (2014). Since our experiments were performed in carbon-saturated conditions by enclosing samples in graphite capsules (See Appendix 1), there is no upper limit on the amount of carbon in the resulting experiments, and hence, these C/O ratios merely signify lower limits. We also chose a third bulk composition (hereafter, TC) resembling solar system terrestrial planetesimals at 1 AU and 0.15 Myr after disk formation from the EC model of Moriarty *et al.* (2014). The TC composition is also saturated with carbon.

2.2. Starting materials

Starting materials were mixed in proportions shown in Table 1. In the first step, SiO_2 (99.9% SiO_2 powder from

Alfa-Aesar), MgO (99.95% MgO powder from Alfa-Aesar), Al_2O_3 (99.95% min alpha Al_2O_3 powder from Alfa-Aesar), $CaCO_3$ (99.95–100.05% ACS chelometric standard $CaCO_3$ powder from Alfa-Aesar), and Fe_2O_3 (99.9% Fe_2O_3 powder from Alfa-Aesar) were homogenized in an agate mortar under ethanol. The oxide/carbonate mixture was decarbonated and reduced in a box furnace by first gradually increasing the temperature from 873 to 1273 K in 6 h. The decarbonated mixture, placed in a platinum crucible, was then heated to 1823 K in a box furnace for 30 min and then quenched to room temperature by immersing the bottom of the platinum crucible in water, leading to the formation of glassy material. It was then ground to a homogeneous powder with an agate mortar under ethanol. Fe (99.95% Fe powder, spherical, <10 micron from Alfa-Aesar), FeS (99.9% FeS powder from Alfa-Aesar), C (99.9995% ultra F purity graphite from Alfa-Aesar), and SiC (≥97.5% SiC powder from Sigma-Aldrich) were added to the powder. The final mixture was again homogenized by grinding in an agate mortar and stored in an oven at 383 K until use.

2.3. High-pressure high-temperature experiments

Experiments summarized in Table 2 were conducted in an end-loaded piston-cylinder apparatus at Vrije Universiteit Amsterdam in a 12.7-mm (half-inch)-diameter cylindrical sample assembly. Details on sample assembly preparation are given in Appendix 1 and Appendix Fig. A1. Pressure and temperature conditions of 1–2 GPa and 1523–1823 K were chosen to represent the interior conditions of Pluto-mass planetesimals and planets. To reduce the porosity of the graphite capsules, the sample assembly was sintered at 1073 K and 1 GPa for 1 h before further heating and pressurization. During heating to the run temperature, the pressure was increased continuously with the hot-piston-in technique (McDade *et al.*, 2002). The temperature was increased at a rate of 100 K/min. The experiments were run for the duration of 3.5–100 h (Table 2). All experiments were quenched to <450 K within ∼15 s by switching off the electric power to the heater.

2.4. Analytical procedure

The recovered samples were mounted in one-inch-diameter mounts with petropoxy resin, cut longitudinally, polished with grit-paper, and fine-polished down to a 1/4 μm

TABLE 1. PLANETESIMAL BULK COMPOSITIONS AND STARTING MATERIALS

Element	SC	EC	TC	Material	SC	EC	TC
Si (mol%)	11.4	9.0	15.3	SiO_2 (wt%)	30.1	19.0	36.7
Mg (mol%)	11.4	9.3	15.3	MgO (wt%)	20.2	19.0	24.6
O (mol%)	45.8	30.0	51.2	FeO[a] (wt%)	27.3	23.1	8.1
Fe (mol%)	11.4	7.6	12.8	Fe (wt%)	2.2	0.0	14.2
S (mol%)	1.9	1.3	3.6	FeS (wt%)	7.0	8.8	12.6
Al (mol%)	1.4	0.9	1	Al_2O_3 (wt%)	3.1	2.4	2.1
Ca (mol%)	0.7	0.5	0.8	CaO[a] (wt%)	1.7	1.5	1.7
C (mol%)	16.0	41.4	—	C (wt%)	8.4	23.5	—
C/O (mol/mol)	0.35	1.38	—	SiC (wt%)	0.0	5.6	—

[a]CaO and FeO are obtained from $CaCO_3$ and Fe_2O_3 after decarbonation and reduction.
SC = sequential condensation chemistry, EC = equilibrium chemistry, TC = third bulk composition based on equilibrium chemistry.

TABLE 2. EXPERIMENTAL CONDITIONS AND RUN PRODUCT PHASES

Run	P (GPa)	T (K)	t (h)	$\log f_{O_2}$ ΔIW	Run product phases (proportions in wt%) (Graphite is an additional phase in all runs)
SC					
1B1t	1	1823	3.5	−0.5	Olv (25%) + SiL (61%) + SrFeL2 (13%)
1B1p	2	1823	3.5	−0.7	Olv (27%) + SiL (56%) + SrFeL2 (18%)
1B1f	1	1723	4	−0.6	Olv (38%) + SiL (46%) + SrFeL2 (16%)
1B1j	2	1723	4	−0.4	Olv (44%) + SiL (46%) + SrFeL2 (10%)
1B1q	1	1623	20	−0.5	Olv (68%) + SiL (21%) + Spi (0.2%) + SrFeL2 (10.8%)
1B1w	2	1623	29	−0.3	Olv (47%) + SiL (41%) + SrFeL2 (11%)
1B1r	1	1545	20	*−0.5*	Olv (74%) + Spi (11%) + CPx (4%) + SrFeL2 (11%)
EC					
2C1a	1	1823	4	−1.2	Olv (41%) + SiL (36%) + SpFeL (9%) + SrFeL (14%)
2C1d	2	1823	4	−1.0	Olv (25%) + SiL (15%) + OPx (36%) + SpFeL (9%) + SrFeL (15%)
2C1e	1	1723	4	−1.2	Olv (30%) + SiL (13%) + OPx (31%) + SpFeL (9%) + SrFeL (17%)
2C1c	2	1723	6	*−0.9*	Olv (36%) + SiL[a] + CPx (41%) + SpFeL (9%) + SrFeL (14%)
TC					
1A2y	1	1823	3.5	−1.1	Olv (38%) + SiL (39%) + SpFeL (14%) + SrFeL (8%)
1A2zc	2	1823	6.5	−1	Olv (26%) + SiL (21%) + OPx (28%) + SpFeL (15%) + SrFeL (10%)
1A2zd	1	1723	8	−1.1	Olv (35%) + SiL (41%) + SpFeL (14%) + SrFeL (9%)
1A2a	2	1723	4	−1	Olv (22%) + SiL[a] + OPx (52%) + SpFeL (15%) + SrFeL (11%)
1A2c	1	1623	4	*−1.2*	Olv (18%) + SiL[a] + OPx (56%) + SpFeL (15%) + SrFeL (12%)
1A2za	2	1623	29	*−1.2*	Olv (28%) + OPx (46%) + SpFeL (15%) + SrFeL (11%)
1A2s	1	1523	100	*−1.0*	Olv (49%) + OPx (20%) + CPx (7%) + FeS (24%)

Oxygen fugacity is calculated assuming a nonideal solution behavior of S-rich Fe alloy and silicate melt (see Appendix 2 for details). Oxygen fugacities in italics are calculated by using olivine instead of silicate melt.

[a]Silicate melt was present in small quantities that could not be measured using EPMA.

CPx = clinopyroxene; EPMA = Electron Probe Micro-Analyzer; FeS = Fe-S solid (single alloy); IW = iron-wüstite; Olv = olivine; OPx = orthopyroxene; SiL = silicate melt; Spi = spinel; SpFeL = S-poor Fe melt; SrFeL = S-rich Fe melt; SrFeL2 = S-rich Fe melt (single alloy).

finish. The polished samples were carbon coated to ensure electrical conductivity of the surface during electron probe microanalysis. Major element contents of the experimental charges were determined with wavelength dispersive spectroscopy on the 5-spectrometer JEOL JXA-8530F Hyperprobe Electron Probe Micro-Analyzer (EPMA) at The Netherlands National Geological Facility, Utrecht University. We used a series of silicate, oxide, and metal standards and conditions of 15 nA beam current and 15 kV accelerating voltage. Analyses were made with a defocused beam to obtain the compositions of metal (2–10 μm diameter) and silicate (5–20 μm diameter) phases. Standards for the quantitative analysis of Mg, Fe, Si, Al, and Ca in silicate minerals were forsterite, hematite, forsterite, corundum, and diopside, respectively, and the standard for Fe in iron alloys was Fe-metal. Counting times were 30 s for Fe (hematite and Fe-metal), Si, Mg, and Al, and 20 s for Ca and S. Quantitative analysis of Pt, with the help of a Pt-metal standard, was also performed to assess contamination from the Pt capsule. To measure light element abundances in iron alloys, the carbon coating was removed and the samples and standards (natural troilite for S, pure Si metal for Si, magnetite for O, and experimentally synthesized Fe_3C for C) were Al coated together for each run to keep the X-ray absorption uniform. These analyses were performed with a JEOL JXA 8530F Hyperprobe at Rice University, Houston, following the analytical protocol of Dasgupta and Walker (2008). Detection limits (3σ) of all elements are less than 0.03 wt% except for Pt (0.07 wt%). Data reduction was performed using the Φ(rZ) correction (Armstrong, 1995). Instrument calibrations were deemed successful when the

composition of secondary standards was reproduced within the error margins defined by the counting statistics.

3. Experimental Observations

3.1. Phase assemblages and texture

Run product phases are listed in Table 2. A clear segregation into silicate and iron-rich phases can be seen in all three series of run products (Fig. 1). Resulting phase diagrams for experiments with SC, EC, and TC compositions are compared with each other in Fig. 2. Oxygen fugacities of EC runs are lower than those of SC runs by an average value of 0.6 log units (Table 2) since sequential condensation models of Moriarty *et al.* (2014) are richer in oxygen than EC models. The oxygen fugacities of carbon-saturated experiments with EC and TC compositions are similar because the relative elemental abundances of EC models, excluding carbon, for HD19994 and the Sun are largely the same (Table 1). Mass balance calculations on iron alloys and silicate phases, excluding graphite, result in 10–18 wt% of iron alloys in SC runs and 23–27 wt% of iron alloys in EC/TC runs.

In our run products, graphite grains <1–100 μm in diameter (Fig. 1a, b, d) were identified with energy dispersive X-ray spectroscopy analyses showing a clear peak of carbon with no other elements. In EC runs with 5 wt% SiC in their starting material, we did not find any SiC grains, suggesting the formation of graphite via the oxidation of silicon in SiC (see Hakim *et al.*, 2018b). Since our experiments were conducted in graphite capsules, all our run products are graphite saturated, and hence, graphite is a stable phase in all runs.
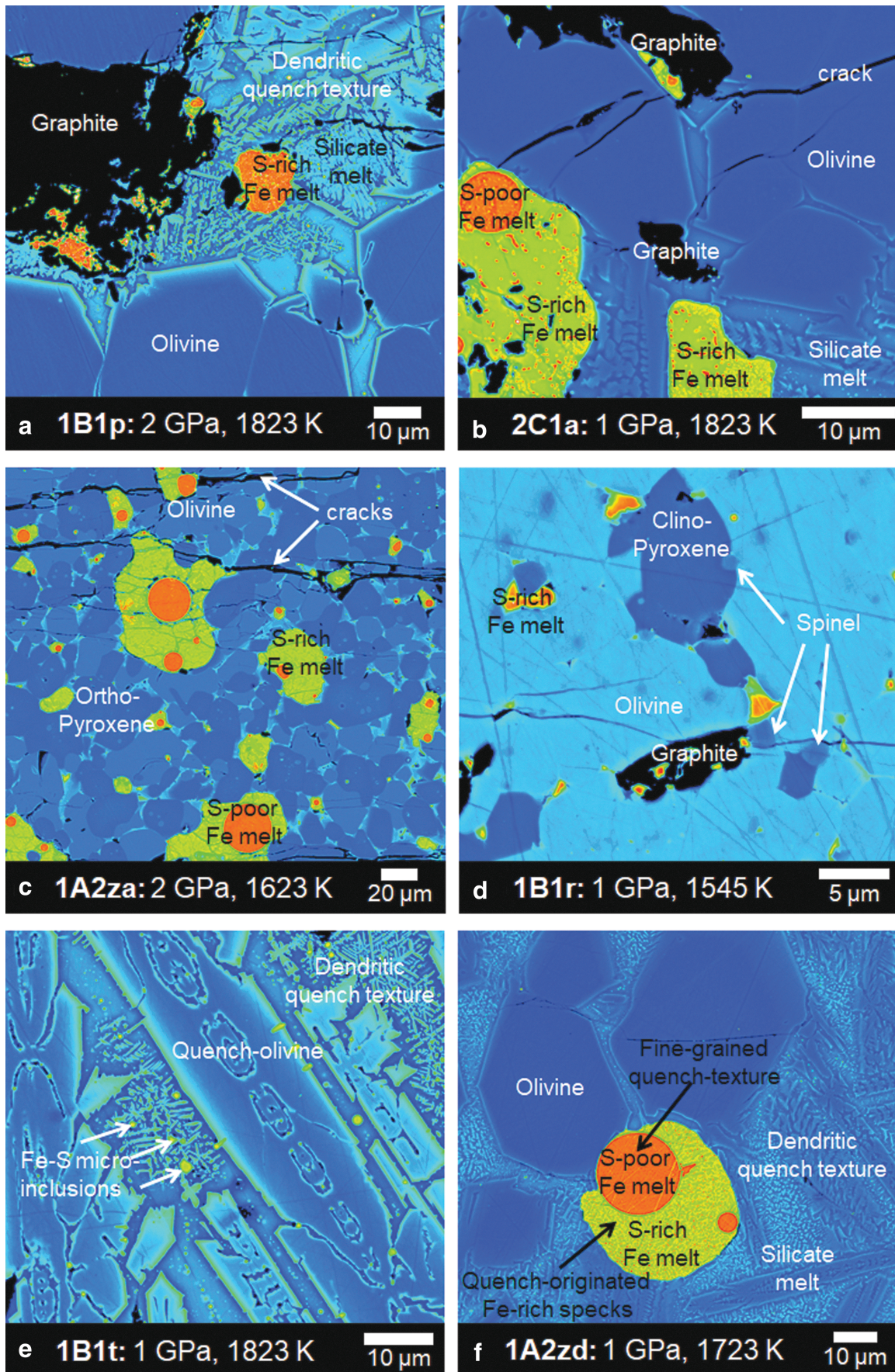
FIG. 1. False-color backscattered electron images of six representative run products (a–f) illustrating different phases and textural types. See text for detailed explanation. Phases can be broadly categorized into graphite, iron alloys, and silicate phases. Silicate melts show a typical dendritic quench texture. Iron alloys show a fine-grained quench texture.
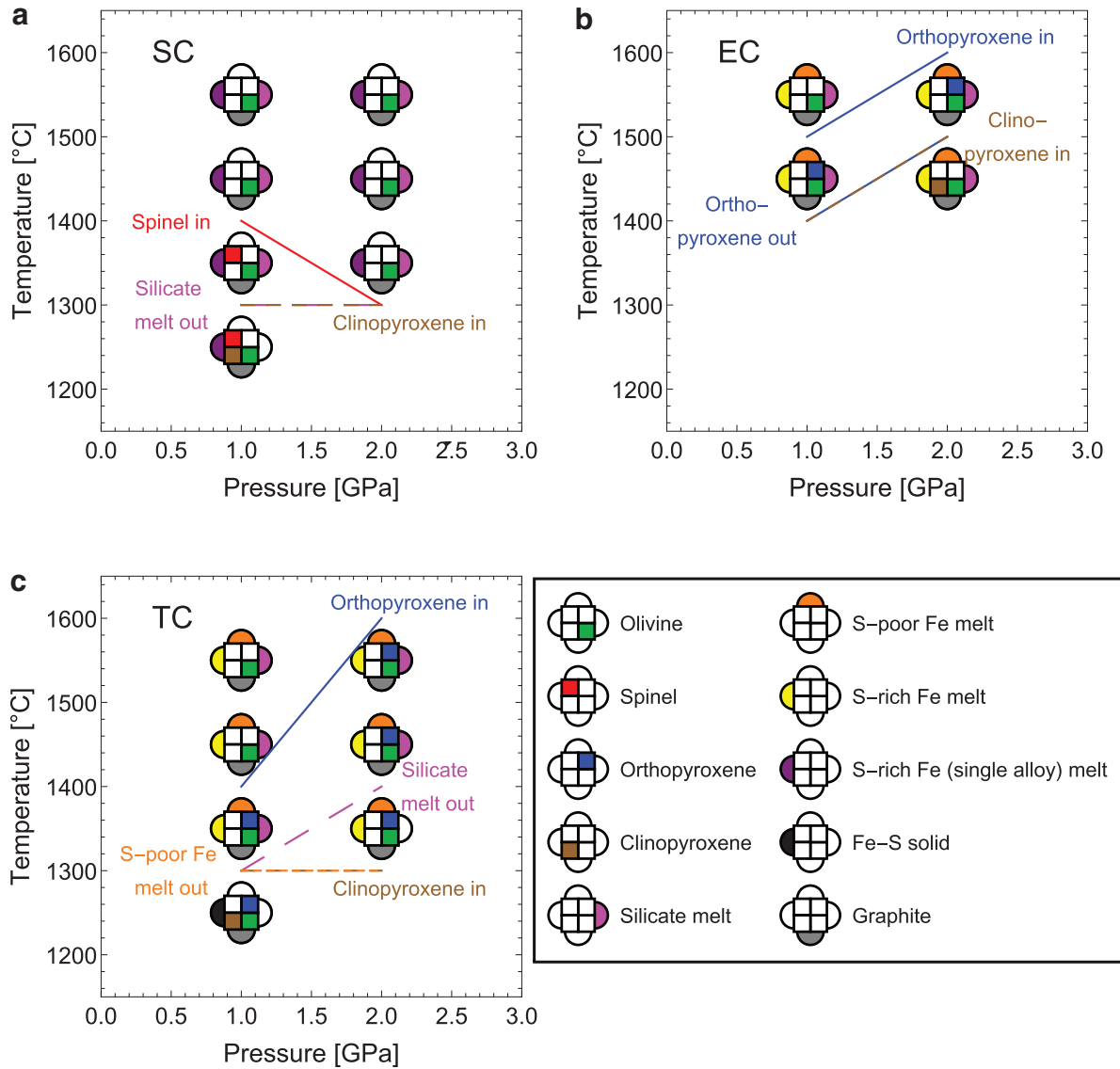
5

FIG. 2. Phase diagrams of SC (**a**), EC (**b**), and TC (**c**) run products. Solid and dashed lines represent major phase changes in the direction of lower temperatures. SC = sequential condensation chemistry, EC = equilibrium chemistry, TC = third bulk composition based on equilibrium chemistry.

Olivine crystals are present in all runs. Orthopyroxene is present in all EC runs except the run at 1 GPa and 1823 K, and in all TC runs except the runs at 1 GPa and 1723–1823 K. The absence of orthopyroxene in SC runs is due to their higher oxygen fugacities and the corresponding higher FeO content. Clinopyroxene is present only at 1 GPa and the lowest temperature in all three series. In SC runs at 1 GPa and 1545–1623 K, spinel is also identified. Silicate melts and iron alloys are usually concentrated between the boundaries of silicate crystals and at the top or edges of capsules. The proportion of silicate melt increases with temperature and decreases with pressure. The solidus of silicate melt in SC runs is lower than in EC/TC runs due to higher oxygen fugacities and the corresponding higher FeO content.

Iron alloys are present in all runs. In all EC/TC runs except the TC run at 1 GPa and 1523 K containing solid Fe-S, two immiscible iron-rich melts (S-rich Fe melt and S-poor Fe melt) are identified. S-poor Fe melt is observed as almost spherical blebs usually surrounded by S-rich Fe melt (Fig. 1b, c, f). This immiscibility is attributed to the chemical interactions between carbon and sulfur. Such liquid metal immiscibility in Fe-C-S systems has been observed for a range of S/Fe ratios in previous studies (*e.g.*, Wang *et al.*, 1991; Corgne *et al.*, 2008; Dasgupta *et al.*, 2009). The S/Fe ratio in iron-rich melts of our EC/TC runs is within this range (Section 3.2). In contrast, SC runs do not exhibit liquid metal immiscibility and contain a single alloy of S-rich Fe melt, since the S/Fe ratio in this series is beyond the range where immiscibility exists (see Section 3.2).

As a result of quenching, the silicate melt exhibits a dendritic texture as shown in Fig. 1a, b, e, and f. Dendrites in SC runs (*e.g.*, Fig. 1a, e) are 5–10 times larger than in EC/TC runs (*e.g.*, Fig. 1b, f). Quenching also results in the growth of thin rims at the boundaries of silicate crystals (*e.g.*, Fig. 1a). These thin rims sometimes have a saw-toothed edge and are thicker in SC runs than in EC/TC runs,

perhaps due to different viscosities and consequently the transport properties of the melts involved owing to different oxygen fugacities (*e.g.*, Giordano *et al.*, 2008). These textures are observed in melt regions because quenching is a non-instantaneous process leading to rapid exsolution and crystallization of melt. The silicate melt also contains Fe-S micro-inclusions resulting from the exsolution of the original melt on quenching (Fig. 1e), similar to observations made in the study of Boujibar *et al.* (2014).

The iron-rich melts show a fine-grained quench texture supporting the interpretation of a liquid state during the experiments. In EC/TC runs, the immiscibility of S-poor and S-rich Fe melts is evident from the sharp boundaries between them (Fig. 1a, c, f). Submicron-sized iron-rich specks seen in S-rich Fe melt, surrounding the S-poor Fe blebs, are likely a result of unmixing on quenching.

3.2. Phase compositions

Tables 3 and 4 list the compositions of silicate and iron-rich phases, respectively. The lithophile elements, Mg, Si, Al, and Ca, are bonded to oxygen in silicate phases. O is largely present in silicate phases and to a smaller extent in iron-rich melts. S mainly partitions into iron-rich phases with smaller amounts present in silicate melts. Fe is distributed among silicate and iron-rich phases. Most of the carbon is present as graphite and a smaller amount is present in iron alloys.

Olivine crystals and silicate melts in EC/TC runs are richer in MgO and poorer in FeO than in SC runs. The Mg# or Mg/(Mg+Fe) mol% of olivine in EC/TC and SC runs is between 75–87 and 55–75, respectively. Similarly, the Mg# of silicate melt in EC/TC and SC runs is between 60–65 and 25–50, respectively. Orthopyroxene, found only in certain EC/TC runs, has Mg# between 80 and 87. The SiO_2 content of silicate melt in EC/TC runs (44–50 wt%) is higher than in SC runs (33–41 wt%). These differences between EC/TC and SC runs are a direct consequence of lower oxygen fugacities of EC/TC runs ($\log f_{O_2} \sim IW - 1.1$) compared with SC runs ($\log f_{O_2} \sim IW - 0.5$) (Table 2). The MgO content of olivine, orthopyroxene, and silicate melt increases and the FeO content decreases with temperature.

Since olivines do not accommodate significant amounts of the oxides of Ca and Al, they are present only in silicate melt and/or pyroxenes. Orthopyroxenes and clinopyroxenes contain a combined 2–5 and 10–25 wt% of CaO and Al_2O_3, respectively. The similarity in CaO and Al_2O_3 contents of clinopyroxenes between SC and EC runs and their differences from TC runs are due to the differences in starting Ca/Si and Al/Si ratios. Silicate melts contain 0.1–0.8 wt% S, with higher values of S seen mainly in SC runs, which is likely due to their higher FeO contents than in the EC/TC runs (*e.g.*, Smythe *et al.*, 2017). The formation of spinel in the SC run at 1 GPa and 1545–1623 K and its absence in TC runs is likely due to a higher Al/Si ratio of the SC composition.

Across EC/TC runs exhibiting liquid metal immiscibility, the S-poor Fe melt contains 86–94 wt% Fe, 3.9±0.9 wt% C, 1.3±0.3 wt% S, and 0.3±0.1 wt% O. The variable Fe content is a result of the variable Pt contamination of 0–8 wt% (0–2 mol%) from the outer Pt capsules surrounding the inner graphite capsules. The S-rich Fe melt contains 69.2±0.5 wt% Fe, 0.8±0.5 wt% C, 29.5±1.1 wt% S, and 1.0±0.3 wt% O. The S-rich Fe melt (single alloy) in SC runs contains

62.7±0.9 wt% Fe, 0.4±0.1 wt% C, 29–37 wt% S, and 1–7 wt% O (~36 wt% S+O, equivalent to sulfur's composition in iron sulfide). The higher amount of oxygen in SC iron alloys is likely due to their higher oxygen fugacity with respect to EC/TC iron alloys.

Figure 3 illustrates that our measurements of S-rich and S-poor Fe melts exhibiting immiscibility are in excellent agreement with the studies of Corgne *et al.* (2008) and Dasgupta *et al.* (2009). The single alloys from our SC runs are clustered together in the lower left corner of Fig. 3 and their composition is a reflection of the starting composition, as is the case for single alloys reported in the work of Corgne *et al.* (2008) and Dasgupta *et al.* (2009). The molar S/Fe ratio in bulk iron-rich melts of our SC runs is ~0.85, which is higher than that of our EC and TC runs having ~0.4 and ~0.25, respectively. Up to pressures of 4–6 GPa, Dasgupta *et al.* (2009) observed immiscibility for S/Fe ratios of ~0.1 and ~0.33 and miscibility for S/Fe ratios of 0.02 and 0.06. Corgne *et al.* (2008) also found immiscibility at S/Fe ~0.15. Since the miscibility gap closes above 4–6 GPa, some runs contain single alloys despite having characteristic S/Fe ratios. Combined with our results, this implies that immiscibility is observed in the Fe-C-S system for moderate S/Fe ratios between ~0.1 and 0.8 up to pressures of 4–6 GPa. For lower or higher S/Fe ratios, a single iron-rich melt is expected.

4. Mineralogy and Structure of C-Enriched Rocky Exoplanets

4.1. Mineralogy

Although our experimental conditions are valid for the interior of Pluto-mass planets as the shallow upper mantles of larger planets, here we discuss mineralogy in the context of both smaller and larger planets. Our experiments show that silicate minerals, iron-rich alloys, and graphite dominate the mineralogy in differentiated C-enriched planetary interiors. In addition to the C/O ratio, the oxygen fugacity and the Mg/Si, Al/Si, Ca/Si, and S/Fe ratios play an important role in determining the mineralogy in carbon-rich conditions. Our oxygen fugacity conditions ($IW - 0.3 < \log f_{O_2} < IW - 1.2$) are a direct reflection of the chemical modeling of Moriarty *et al.* (2014) who calculated the bulk composition of planetesimals in protoplanetary disks. However, oxygen fugacity can vary over a larger range either because of its dependence on pressure implying its change with depth in planetary interiors, or due to the formation in protoplanetary disks of more reducing bulk compositions than the ones used in this study. Here we place our results in a broader context of C-enriched planetary interiors by combining our results with previous studies.

At $IW < \log f_{O_2} < IW - 2$ and up to ~4–6 GPa, our study and previous studies (*e.g.*, Dasgupta *et al.*, 2009, 2013) show that iron-rich melts are composed of single alloys or two immiscible alloys in the Fe-C-S system depending on the S/Fe ratio. The immiscible S-poor and S-rich Fe melts show characteristic solubilities with ~5 wt% C and ~1 wt% S, and ~1 wt% C and ~30 wt% S, respectively. At pressures higher than ~4–6 GPa, a closure of the miscibility gap will allow only single Fe-C-S alloys (Corgne *et al.*, 2008; Dasgupta *et al.*, 2009). With decreasing $\log f_{O_2}$ from $IW - 2$ to $IW - 6$, the solubility of C in Fe decreases and the solubility of Si in Fe increases (Deng *et al.*, 2013; Li *et al.*, 2016). At

TABLE 3. COMPOSITION OF SILICATE PHASES FORMED IN EXPERIMENTAL RUN PRODUCTS

Run	n	SiO₂	MgO	FeO	Al₂O₃	CaO	S	Sum	K_D	K'_D
Olivine										
1B1t	19	38.5 (0.1)	39.9 (0.1)	21.3 (0.1)	0.1 (0.0)	0.1 (0.0)	<DL	99.9 (0.1)	0.26	0.26
1B1p	10	38.2 (0.1)	40.0 (0.1)	20.9 (0.2)	0.1 (0.0)	0.1 (0.0)	<DL	99.3 (0.1)	0.32	0.28
1B1f	12	37.6 (0.1)	37.7 (0.1)	23.7 (0.1)	0.1 (0.0)	0.1 (0.0)	<DL	99.3 (0.1)	0.27	0.26
1B1j	10	36.5 (0.1)	34.5 (0.3)	28.5 (0.5)	0.1 (0.0)	0.2 (0.0)	<DL	99.9 (0.3)	0.3	0.26
1B1q	10	35.3 (0.1)	29.8 (0.4)	34.0 (0.1)	0.2 (0.2)	0.3 (0.1)	<DL	99.5 (0.2)	0.25	0.27
1B1w	10	37.0 (0.1)	34.5 (0.2)	27.5 (0.2)	0.1 (0.0)	0.2 (0.0)	<DL	99.4 (0.1)	0.25	0.25
1B1r	9	35.4 (0.3)	28.2 (0.3)	35.0 (0.1)	0.6 (0.5)	0.4 (0.1)	<DL	99.5 (0.3)	—	—
2C1a	9	39.4 (0.1)	48.0 (0.1)	12.9 (0.1)	0.1 (0.0)	0.1 (0.0)	<DL	100.5 (0.1)	0.24	0.29
2C1d	10	39.7 (0.1)	43.7 (0.3)	17.6 (0.1)	0.2 (0.2)	0.2 (0.1)	<DL	100.5 (0.2)	0.38	0.28
2C1e	10	38.6 (0.1)	44.7 (0.6)	16.1 (0.7)	0.2 (0.2)	0.2 (0.0)	<DL	99.8 (0.4)	0.26	0.28
2C1c[a]	10	38.0 (0.2)	39.7 (0.2)	21.5 (0.3)	0.5 (0.2)	0.2 (0.0)	<DL	99.9 (0.2)	—	—
1A2y	10	40.3 (0.3)	44.7 (0.1)	15.0 (0.1)	0.0 (0.0)	0.1 (0.0)	<DL	100.2 (0.2)	0.31	0.28
1A2zc	9	39.9 (0.1)	42.8 (0.1)	16.7 (0.1)	0.1 (0.0)	0.1 (0.0)	<DL	99.5 (0.1)	0.35	0.28
1A2zd	11	39.9 (0.2)	45.2 (0.5)	14.3 (0.5)	0.0 (0.0)	0.1 (0.0)	<DL	99.6 (0.3)	0.31	0.28
1A2a[a]	8	38.4 (0.2)	41.9 (0.3)	19.6 (0.2)	0.1 (0.0)	0.2 (0.0)	<DL	100.2 (0.2)	—	—
1A2c[a]	7	37.5 (0.3)	42.4 (0.5)	19.5 (0.1)	0.1 (0.0)	0.3 (0.0)	<DL	99.9 (0.3)	—	—
1A2za	17	39.7 (0.1)	40.5 (0.2)	19.7 (0.1)	0.1 (0.0)	0.2 (0.0)	<DL	100.3 (0.1)	—	—
1A2s	8	38.6 (0.1)	40.7 (0.2)	20.3 (0.3)	0.1 (0.0)	0.2 (0.0)	<DL	99.8 (0.2)	—	—
Orthopyroxene										
2C1d	8	54.8 (0.2)	30.8 (0.4)	10.7 (0.4)	3.0 (0.4)	0.9 (0.1)	<DL	100.3 (0.3)	0.32	
2C1e	8	56.4 (0.6)	31.8 (0.2)	9.5 (0.1)	2.0 (0.4)	0.8 (0.0)	<DL	100.6 (0.3)	0.22	
1A2zc	10	56.4 (0.1)	30.8 (0.1)	10.9 (0.1)	0.9 (0.0)	0.7 (0.0)	<DL	99.8 (0.1)	0.32	
1A2a[a]	8	54.8 (0.1)	29.8 (0.5)	12.2 (0.1)	2.0 (0.2)	1.2 (0.1)	<DL	100.0 (0.2)	—	
1A2c[a]	8	53.7 (0.9)	30.4 (0.4)	12.1 (0.2)	2.3 (0.1)	1.3 (0.1)	<DL	99.8 (0.5)	—	
1A2za	17	55.8 (0.5)	28.6 (0.4)	12.4 (0.3)	2.3 (0.4)	1.5 (0.2)	<DL	100.7 (0.3)	—	
1A2s	7	53.3 (1.2)	28.9 (0.6)	12.1 (0.4)	3.1 (0.5)	2.1 (0.1)	<DL	99.5 (0.7)	—	
Clinopyroxene										
1B1r	10	48.6 (0.4)	20.0 (0.4)	21.1 (0.1)	7.3 (0.6)	2.4 (0.4)	<DL	99.4 (0.4)		
2C1c[a]	4	51.2 (0.4)	25.3 (0.4)	13.8 (0.4)	7.5 (0.6)	2.3 (0.1)	<DL	100.0 (0.4)		
1A2s	8	49.2 (0.5)	17.8 (1.0)	7.3 (0.2)	9.3 (0.9)	15.8 (1.0)	<DL	99.4 (0.8)		
Spinel										
1B1q	8	0.3 (0.1)	13.3 (0.1)	24.6 (0.2)	60.9 (0.3)	0.1 (0.0)	<DL	99.1 (0.2)		
1B1r	7	0.7 (0.4)	12.9 (0.2)	27.3 (0.1)	58.6 (0.6)	0.1 (0.0)	<DL	99.6 (0.4)		
Silicate melt										
1B1t	9	37.0 (0.5)	17.0 (1.2)	34.2 (1.1)	6.1 (0.7)	3.2 (0.3)	0.7 (0.2)	98.1 (0.8)		
1B1p	10	41.9 (0.4)	17.0 (0.5)	27.9 (0.5)	6.6 (0.3)	3.2 (0.1)	0.6 (0.1)	97.0 (0.3)		
1B1f	10	39.6 (0.3)	13.5 (0.4)	31.2 (0.4)	7.4 (0.2)	4.2 (0.1)	0.8 (0.1)	96.8 (0.3)		
1B1j	8	33.5 (0.5)	14.0 (1.8)	38.9 (1.5)	7.2 (1.3)	3.4 (0.6)	0.4 (0.0)	97.4 (1.1)		
1B1q	10	38.2 (0.3)	7.0 (0.7)	32.0 (0.3)	12.8 (0.3)	7.1 (0.2)	0.6 (0.0)	97.8 (0.4)		
1B1w	11	33.9 (0.3)	12.0 (1.4)	38.5 (0.6)	8.9 (1.0)	4.1 (0.5)	0.8 (0.2)	98.1 (0.8)		
2C1a	6	50.0 (1.4)	15.2 (2.5)	17.3 (1.4)	9.2 (1.2)	5.3 (0.6)	0.3 (0.1)	97.2 (1.4)		
2C1d	6	43.7 (1.9)	19.7 (3.7)	21.0 (1.3)	8.7 (2.1)	4.9 (1.0)	0.1 (0.0)	98.1 (2.0)		
2C1e	8	48.4 (1.0)	11.3 (2.5)	15.7 (1.1)	13.4 (1.6)	8.0 (0.8)	0.2 (0.0)	97.0 (1.4)		
1A2y	14	50.6 (0.5)	18.8 (1.7)	20.6 (0.8)	5.2 (0.3)	4.1 (0.3)	0.4 (0.1)	99.7 (0.8)		
1A2zc	11	45.4 (0.7)	19.9 (0.4)	22.1 (0.5)	6.1 (0.2)	4.8 (0.2)	0.3 (0.1)	98.7 (0.4)		
1A2zd	10	50.8 (0.5)	19.6 (0.9)	19.7 (0.4)	4.8 (0.3)	3.7 (0.3)	0.3 (0.1)	99.1 (0.5)		

All compositions are in wt% with 1σ error given in parentheses. Sulfur in silicate melts is reported as S since oxygen fugacities are much lower than needed to form sulfates (Jugo *et al.*, 2005; Jugo *et al.*, 2010). Runs marked [a] contain silicate melt in small quantities but could not be measured using EPMA. *n* is the number of analytical points. DL: detection limit. Pt is <DL in all silicate phases. K_D is the olivine/silicate melt FeO-MgO exchange coefficient and K'_D is the corrected exchange coefficient from Toplis (2005) (see Appendix 3 for mineral/melt equilibrium calculations).

even lower oxygen fugacities (log $f_{O_2} \sim$ IW − 6.2), C is not soluble in Fe and about 20 wt% Si is present (Takahashi *et al.*, 2013). Morard and Katsura (2010) show that the Fe-S-Si system also exhibits liquid metal immiscibility similar to the Fe-C-S system at log $f_{O_2} \sim$ IW − 10, although this miscibility gap closes at ∼25 GPa. If the temperature is lower than the liquidus in the Fe-C±S±Si system, solids such as Fe, FeS, Fe₃C, Fe₇C₃, and Fe-Si can form depending on pressure and f_{O_2} (Deng *et al.*, 2013).

Takahashi *et al.* (2013) found olivine to be a dominant silicate mineral in the FMS+CO system at IW − 1 < log f_{O_2} < IW−3.3 and 4 GPa. Our experiments in the FCMAS+CSO system at IW − 0.3 < log f_{O_2} < IW−1.2 and 1–2 GPa showed a larger variety in silicate minerals such as orthopyroxene, clinopyroxene, and spinel, in addition to olivine. The diversity in silicates increases with decreasing temperature. The compositions of these silicate minerals are sensitive to f_{O_2} and Mg/Si, Ca/Si, and Al/Si ratios. At their lowest

TABLE 4. COMPOSITION OF IRON-RICH PHASES FORMED IN EXPERIMENTAL RUN PRODUCTS

Run	n/m	Fe	Pt	Si	C	S	O	Sum
S-rich Fe melt (single alloy)								
1B1t	10/4	62.7 (0.3)	0.4 (0.3)	0.4 (0.5)	0.7 (0.4)	29.1 (0.6)	5.7 (0.8)	98.9 (0.5)
1B1p	12/5	61.1 (0.6)	1.6 (0.4)	0.1 (0.1)	0.5 (0.2)	33.6 (1.3)	3.5 (2.9)	100.5 (0.7)
1B1f	8/10	62.6 (0.2)	0.3 (0.2)	0.1 (0.1)	0.4 (0.2)	30.3 (0.9)	5.1 (0.8)	98.8 (0.5)
1B1j	9/9	63.0 (0.8)	1.8 (0.4)	0.2 (0.1)	0.5 (0.2)	29.4 (1.2)	6.5 (1.0)	101.3 (0.7)
1B1q	8/8	64.0 (0.3)	0.4 (0.1)	0.1 (0.1)	0.2 (0.1)	28.5 (1.7)	6.0 (1.6)	99.3 (1.0)
1B1w	9/10	63.4 (0.2)	0.1 (0.1)	0.3 (0.1)	0.4 (0.2)	29.4 (0.9)	6.7 (0.6)	100.3 (0.5)
1B1r	8/9	61.9 (1.0)	0.9 (0.8)	<DL	0.3 (0.1)	37.3 (0.2)	0.7 (0.2)	101.1 (0.5)
S-rich Fe melt								
2C1a	5/10	69.2 (0.3)	<DL	<DL	1.0 (0.7)[a]	30.3 (0.2)	0.9 (0.3)[a]	101.4 (0.2)
2C1d	5/10	70.3 (1.4)	0.2 (0.1)	<DL	1.0 (0.7)	27.0 (0.4)	0.9 (0.3)	99.4 (0.6)
2C1e	5/4	68.8 (1.9)	0.1 (0.1)	<DL	1.6 (0.7)	30.2 (1.0)	1.3 (0.8)	102.0 (1.0)
2C1c	5/4	69.4 (1.0)	0.3 (0.1)	<DL	1.6 (0.7)[a]	28.9 (1.2)	1.3 (0.8)[a]	101.6 (0.8)
1A2y	10/10	68.4 (0.3)	<DL	<DL	0.4 (0.2)	29.8 (0.9)	1.0 (0.5)	99.6 (0.4)
1A2zc	7/7	68.6 (0.8)	0.3 (0.1)	<DL	0.6 (0.1)	29.7 (1.6)	1.1 (0.1)	100.3 (0.7)
1A2zd	15/11	69.2 (0.9)	0.3 (0.0)	<DL	0.4 (0.1)	30.2 (1.2)	0.6 (0.2)	101.6 (0.6)
1A2a	14/5	69.3 (1.2)	0.2 (0.1)	<DL	0.4 (0.1)	29.7 (1.4)	0.9 (0.4)	100.7 (0.8)
1A2c	8/10	68.9 (0.9)	0.1 (0.0)	<DL	0.6 (0.2)	30.2 (1.1)	0.6 (0.2)	100.4 (0.6)
1A2za	8/5	69.4 (0.6)	0.3 (0.1)	<DL	0.8 (0.5)	29.4 (0.6)	1.1 (0.2)	100.9 (0.4)
S-poor Fe melt								
2C1a	5/20	94.0 (0.5)	0.5 (0.1)	<DL	3.6 (0.2)	0.9 (0.1)	0.4 (0.0)	99.4 (0.2)
2C1d	5/16	89.0 (0.5)	3.5 (0.1)	<DL	3.2 (0.2)	1.9 (0.1)	0.4 (0.0)	98.0 (0.2)
2C1e	4/5	93.8 (0.5)	0.2 (0.0)	<DL	5.4 (1.0)	1.7 (0.3)	0.4 (0.0)	101.4 (0.5)
2C1c	4/12	88.3 (0.2)	4.4 (0.2)	<DL	4.5 (0.3)	1.1 (0.1)	0.2 (0.0)	98.5 (0.2)
1A2y	13/10	90.9 (0.4)	3.6 (0.4)	<DL	2.1 (0.1)	1.0 (0.1)	0.3 (0.0)	97.8 (0.2)
1A2zc	13/9	87.4 (0.6)	6.4 (0.4)	<DL	3.6 (0.6)	1.4 (0.2)	0.3 (0.0)	99.2 (0.4)
1A2zd	9/11	87.1 (0.3)	6.4 (0.2)	<DL	3.3 (0.2)	1.0 (0.2)	0.2 (0.0)	98.1 (0.2)
1A2a	7/10	88.2 (0.7)	6.4 (0.5)	<DL	4.3 (0.4)	1.3 (0.2)	0.3 (0.0)	100.4 (0.4)
1A2c	10/10	89.1 (0.8)	5.1 (0.8)	<DL	4.5 (0.5)	1.0 (0.2)	0.3 (0.1)	100.0 (0.5)
1A2za	17/13	86.2 (0.5)	8.3 (0.3)	<DL	4.5 (0.9)	1.6 (0.2)	0.2 (0.1)	100.9 (0.4)
Fe-S solid								
1A2s	9/5	61.3 (0.1)	0.2 (0.1)	<DL	0.5 (0.2)	38.9 (0.1)	0.3 (0.1)	101.1 (0.1)

All compositions are in wt% with 1σ error given in parentheses. *n* is the number of analytical points for Fe and Pt, and *m* is the number of analytical points for other elements. DL: detection limit. Mg, Ca, and Al are <DL in all iron-rich phases. The Pt contamination is 0–2.2 mol% in S-poor Fe melt, negligible in S-rich Fe melt, and 0–0.4 mol% in S-rich Fe melt (single alloy). The numbers marked with [a] were not measured for that phase and have been taken from the same phase of another run product at similar conditions.

$\log f_{O_2} < IW - 6.2$, Takahashi *et al.* (2013) found periclase to be a dominant mineral because of decreased concentration of SiO_2. At pressures above 25 GPa, olivine polymorphs break down to form perovskite and ferropericlase (Hirose and Fei, 2002).

We do not observe any carbonates in our runs since magnesite and calcite are stable only at very oxidizing conditions, $\log f_{O_2} > IW + 1$ (Rohrbach and Schmidt, 2011; Lazar *et al.*, 2014). We also do not find silicon carbide in our runs, as it forms only at extremely reducing conditions, $\log f_{O_2} \sim IW - 6.2$ (Takahashi *et al.*, 2013). Only highly reduced planets containing no oxidized iron (Fe^{2+} or Fe^{3+}) can stabilize silicon carbide in their magma ocean stage (see Hakim *et al.*, 2018b). Our starting compositions do not present such extremes in terms of oxygen fugacity and these minerals are therefore unlikely to form in the magma ocean stage of the type of planets we have considered.

Carbon solubility in the interior of the Earth is key in driving the terrestrial carbon cycle (Dasgupta, 2013). Similarly, carbon solubility is expected to impact the carbon cycles and habitability on C-enriched rocky exoplanets (Unterborn *et al.*, 2014). Although we do not measure the carbon abundance in silicate melts of our experiments, Li

et al. (2015, 2016) gave an upper limit of ∼200 ppm C in silicate melts at oxygen fugacity conditions similar to our experiments. The C-solubility in S-poor Fe melts is 3–9 wt% (Boujibar *et al.*, 2014; Rohrbach *et al.*, 2014; Li *et al.*, 2015, 2016, and this study), which is more than two orders of magnitude larger than the C-solubility in silicates.

In Fig. 4, we plot the C-solubility in the mantle and core against core mass percent (excluding graphite) for our experiments and those from the works of Corgne *et al.* (2008) and Takahashi *et al.* (2013). Since all experiments are carbon saturated, this figure essentially gives the minimum amount of carbon in a planet that is necessary to achieve carbon saturation in the planet during its magma ocean stage. For a C-enriched exoplanet with an EC/TC-like composition and 25% of its mass in the core, ∼0.7 wt% C (molar C/O ∼0.03) is sufficient for carbon saturation. For a C-enriched exoplanet with an SC-like composition and 10% of its mass in the core, ∼0.05 wt% C (C/O ∼0.002) is sufficient for carbon saturation. For an extreme case with a core mass of 0, the minimum amount of carbon needed for carbon saturation is 200 ppm (C/O ∼0.001). In contrast, if the core mass percent is Mercury like (70%), assuming 9 wt% C in the core, 6 wt% C (C/O ∼0.5) is needed for carbon saturation. Once carbon
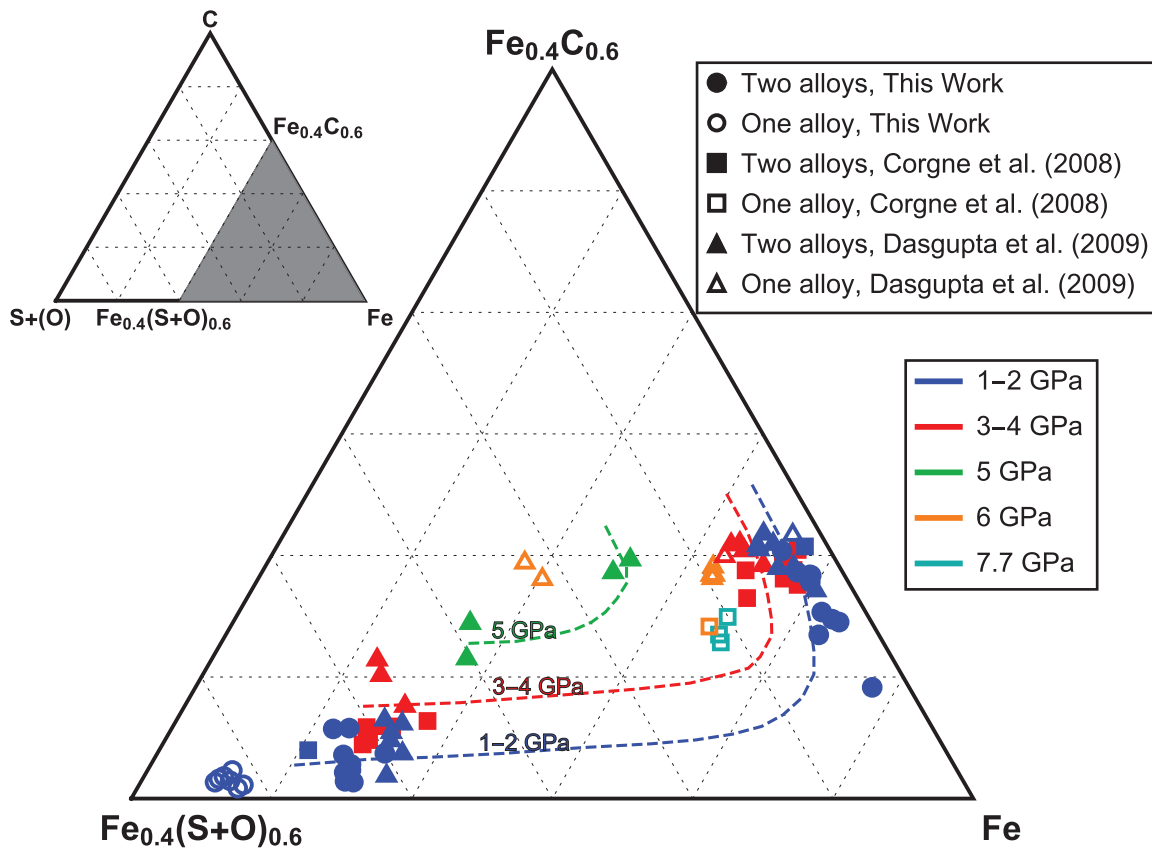
FIG. 3. Liquid metal immiscibility in the Fe-C-S system compared with results from previous studies. For all studies, O measurements are added to S. For Corgne *et al.* (2008), Ni measurements are added to Fe. The hand-drawn dashed lines based on the experiments considered here represent the compositional variation of immiscible S-poor and S-rich Fe melts with pressure.

saturation is achieved, an increase in C/O ratio increases only the amount of graphite produced, and this has a negligible impact on the mineralogy of silicates or iron alloys. The solubilities of carbon for the experiments considered in Fig. 4 are lower than the 9 wt% C-solubility from the work of Boujibar *et al.* (2014) because of the difference in oxygen fugacities and/or the presence of two Fe alloys where S-rich Fe melts have lower C-solubility than S-poor Fe melts, which decreases the net C-solubility in the iron-rich core. The C-solubility in the core is more or less the same for $\log f_{O_2}$ from IW to IW-2, whereas it decreases with a further decrease in $\log f_{O_2}$ from IW-2 to IW-6.2, where it becomes negligible.

4.2. Interior structure

High temperatures during planet formation enable melting and chemical segregation of several minerals (Elkins-Tanton, 2012). These minerals eventually undergo gravitational stratification. For C-enriched rocky exoplanets, iron alloys, silicates, and graphite are the main categories of minerals based on densities. Due to density contrasts of more than 40% between graphite and silicates and more than 50% between silicates and iron alloys, three major gravitationally stable layers are expected to form in these exoplanets: an iron-rich core, a silicate mantle, and a graphite layer on top of the silicate mantle.

For smaller C-enriched rocky exoplanets (with interior pressures <4 GPa) showing Fe-C-S liquid metal immisci-

bility, S-poor Fe alloy will form the inner core and S-rich Fe alloy will form the outer core because of the density contrast between the two alloys. Our mass-balance calculations show that the core/mantle mass ratio would be ~ 0.33 for planets with EC/TC compositions and ~ 0.15 for planets with SC composition. Even though the core/mantle ratio is similar for EC and TC compositions, the S-poor Fe inner-core to the S-rich Fe outer-core mass ratio would be about 0.7 for TC planets and about 1.6 for EC planets owing to a difference in the S/Fe ratio. For C-enriched exoplanets with core pressures larger than 6 GPa, there would be no stratification in the core because of the closure of the miscibility gap. For planets with extremely reducing cores showing Fe-S-Si immiscibility, again an inner and an outer core would exist (*e.g.*, Morard and Katsura, 2010). Depending on composition, pressure, temperature, and f_{O_2}, cores may stratify into multiple metal-rich layers, for instance, a solid Fe_3C inner core with a liquid S-rich Fe outer core, or a solid Fe inner core surrounded by a solid Fe_3C middle core and a liquid FeS outer core (*e.g.*, Deng *et al.*, 2013).

Even though C-enriched rocky exoplanets are expected to contain large amounts of carbon, olivine and pyroxenes would be the common mantle minerals, similar to C-poor rocky planets. In addition, minerals such as spinel and garnet may be abundant in the upper mantle for planets depending on Al/Si and Ca/Si ratios, which might also vary as shown by the models of Carter-Bond *et al.* (2012a). For larger C-enriched rocky exoplanets, high-pressure phases of these

FIG. 4. Experimental measurements of carbon solubility in iron alloys are plotted against the core mass percent. Solid lines give upper bounds on carbon solubility in a molten iron-rich core and a molten silicate mantle.
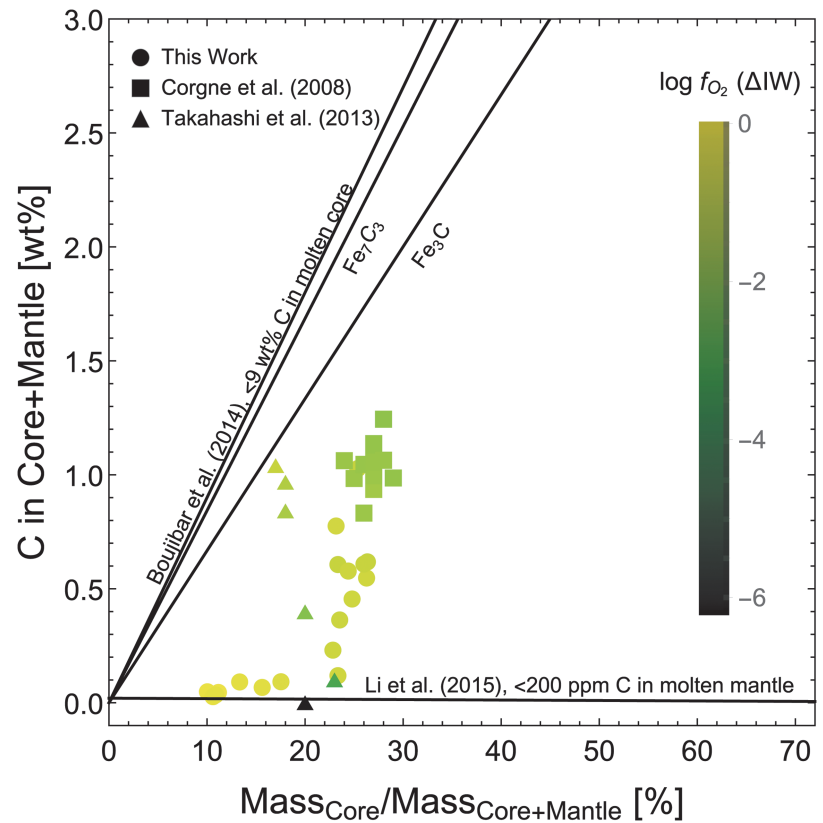
minerals, ferropericlase and perovskite and/or postperovskite, would be the most abundant minerals in the lower mantle.

Graphite will likely form a flotation layer on top of the magma ocean or silicates such as olivine because of its lower density. Graphite is expected to be in its solid state because the melting temperature of the graphite/diamond system exceeds 4000 K for all pressures in a planetary interior (Ghiringhelli *et al.*, 2005). If the graphite layer extends deep into the planet exceeding pressures of 2–15 GPa and depending on the temperature, diamond would form beneath graphite. Since diamond is denser than graphite with a density comparable with some silicate minerals, convection, if it exists, in the mantle may strip off diamonds from beneath the graphite layer. This may result in a diamond/silicate mantle similar to the mantle discussed by Unterborn *et al.* (2014). In addition, the possible presence of metastable states in the carbon system, at conditions near the equilibrium graphite-diamond transition, may have interesting consequences for planetary evolution because of their substantially different physical properties compared with those of graphite and diamond (*e.g.*, Shabalin (2014)). However, the discussion of these metastable states is beyond the scope of this study.

5. A C-Enriched Interior for Kepler-37b

5.1. Effect of a graphite layer on the derived mass

Transit photometry is used to measure the radius of exoplanets (Batalha, 2014). Follow-up stellar radial velocity measurements help to put constraints on their masses, but for most of the rocky exoplanets, masses are currently unknown. Due to graphite's significantly lower density compared with silicate minerals and iron-rich alloys, the mass of an exoplanet in the presence of significant amounts of graphite

would be lower than expected for a given radius. To quantify the effect of graphite on a planet's mass, we compute the interior structure and mass of the smallest known exoplanet till date, Kepler-37b with radius of $0.34\,R_{\oplus}$ (Stassun *et al.*, 2017), by following the isothermal recipe to solve the hydrostatic and Poisson's gravitational gradient equations and keeping the radius fixed (*e.g.*, Unterborn *et al.*, 2016). We implement the third-order Birch-Murnaghan equation of state to provide a relationship between density and pressure (Birch, 1947). Since we are interested in the effect of graphite on its total mass, we assume Kepler-37b is fully differentiated with a pure iron or an iron sulfide core, an enstatite mantle, and a graphite layer. To model the equations of state, we use the thermoelastic data of graphite (Colonna *et al.*, 2011), enstatite (Stixrude and Lithgow-Bertelloni, 2005), iron (Fei *et al.*, 2016), and iron sulfide (Sata *et al.*, 2010).

Applying a core/mantle mass ratio of 0.33, similar to our EC/TC results, and assuming a pure Fe core and an enstatite mantle to the interior structure model of Kepler-37b, the derived mass is 0.26 times the martian mass ($0.26\,M_{\mars}$). When a 33.3 wt% graphite layer is assumed on top of its mantle keeping the core/mantle mass ratio at 0.33, the total mass becomes $0.21\,M_{\mars}$ (about 19% less). In fact, a graphite layer of 10 wt% of the planet's total mass is sufficient to decrease the derived mass of Kepler-37b by 7% (Fig. 5). Assuming a hypothetical 100 wt%, graphite-only planet gives a mass of $0.16\,M_{\mars}$ (about 40% less). For models with an FeS core instead of pure Fe, a similar trend can be seen (Fig. 5).

With current and future missions such as TESS (Ricker *et al.*, 2014), CHEOPS (Fortier *et al.*, 2014), and PLATO (Ragazzoni *et al.*, 2016), the masses and radii of rocky exoplanets will be measured with higher accuracy. Along with improved knowledge of stellar chemistry, tighter
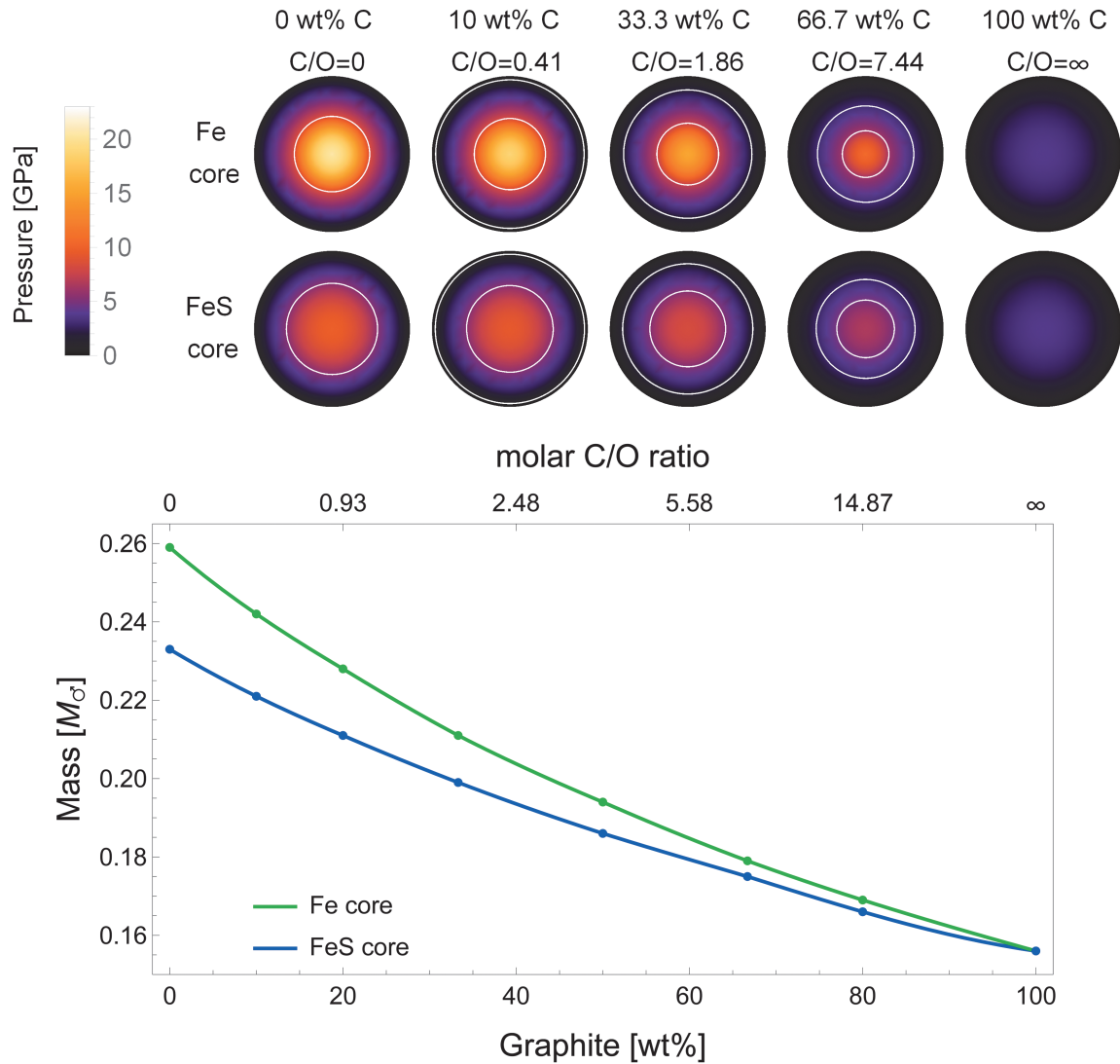
FIG. 5. (Bottom) Solid lines represent the derived mass of Kepler-37b assuming a pure iron or an iron sulfide core, an enstatite mantle, and a graphite crust with a core/mantle mass ratio of 0.33 and different mass fractions of graphite for a fixed planet's radius of 0.34 RC (Stassun *et al.*, 2017). (Top) The internal pressure distribution of Kepler-37b is also shown for five cases where white contours represent the core/mantle and mantle/crust boundaries.

constraints on planetary bulk compositions will also be feasible (Dorn *et al.*, 2015; Santos *et al.*, 2017). This in turn will enable better constraints on the presence of low-density minerals such as graphite in the interior of rocky exoplanets.

We also show the internal pressure distribution of Kepler-37b in Fig. 5 for the cases of 0, 10, 33.3, 66.7, and 100 wt% graphite. The central pressure of Kepler-37b decreases with the amount of graphite. For our models of Kepler-37b, pressures at the bottom of graphite layers are <4 GPa, making phase transformation to diamond impossible at temperatures above 1000 K (Ghiringhelli *et al.*, 2005). C-enriched rocky exoplanets larger than Kepler-37b with thick graphite layers are likely to form diamonds beneath these graphite layers. If the amount of diamond is significantly larger than that of graphite, the effect on the derived mass of the planet would be smaller since the density of diamond is higher than graphite and comparable with silicates.

5.2. Observations and habitability

The abundance of graphite on the planetary surface will have major consequences for planetary thermal evolution, volatile cycles and atmospheric composition, surface geochemistry and habitability. Identification of such a planet by future observations would be of great significance. Graphite has a very low reflectance compared to the usual silicate-rich minerals forming the surface of terrestrial planets such as Mars. If the Earth or an exoplanet is covered with a graphite layer, the planet's surface would likely appear to be dark with an albedo much lower than expected for a C-poor planet. Similarly, a darkening agent discovered on Mercury's surface has been speculated to be graphite (Peplowski *et al.*, 2016).

Small C-enriched exoplanets are unlikely to retain a primary atmosphere. Secondary atmospheres of graphite-layered planets might be nonexistent if the graphite layers are able to completely isolate the silicate mantles. For planets with relatively thin graphite layers, outgassing processes from the

silicate mantle may allow for an atmosphere to exist. Atmospheres of C-enriched rocky exoplanets are believed to be devoid of oxygen-rich gases (*e.g.*, Kuchner and Seager, 2005). Carbon is dissolved in silicate melts mainly as CO_2 at $\log f_{O_2} > IW-1$ and mainly as CH_4 and partially as CO_2 at $\log f_{O_2} < IW-1$ (Li *et al.*, 2015). Future observations of exoplanetary atmospheric gases such as CO/CO_2 or CH_4 may not imply the existence or absence of graphite-rich surfaces.

If the graphite layer is several hundreds of kilometers thick, it might not allow direct recycling of the mantle material to the surface. Such a graphite surface without essential life-bearing elements other than carbon will make the planet potentially uninhabitable. However, deep silicate volcanism, along with the presence of water, could still alter the surface composition of a C-enriched rocky exoplanet during the course of its evolution if penetration of material through the graphite is possible. To further assess these scenarios, detailed studies of the thermal and mechanical behavior of graphite/diamond crusts are required.

6. Summary and Conclusions

We performed the first high-pressure high-temperature experiments on chemical mixtures representing bulk compositions of small C-enriched rocky exoplanets at 1 AU from their host star based on the calculations of a study modeling the chemistry in the protoplanetary disk of a high C/O star. Our results show that fully differentiated C-enriched rocky exoplanets consist of three major types of phases that form an iron-rich core, a silicate mantle, and a graphite (and diamond) layer on top of the silicate mantle. Their mineralogy depends on oxygen fugacity and Mg/Si, Al/Si, Ca/Si, S/Fe, and C/O ratios.

For S/Fe ratios in iron alloys between 0.1 and 0.8 and at pressures below ~ 4–6 GPa, the core stratifies into an S-poor Fe inner core surrounded by an S-rich Fe outer core. The variety in mantle silicate minerals is largely independent of the C/O ratio. The sequential condensation model from the work of Moriarty *et al.* (2014) at 1 AU from the host star results in C-enriched rocky exoplanets with higher oxygen fugacity conditions compared with the equilibrium condensation model. High C/O ratios in planet-forming refractory material do not necessarily imply reducing conditions as the amount of C has no direct impact on the oxygen fugacity. Extremely reducing (<IW−6) or oxidizing conditions (>IW + 1) would be needed to stabilize silicon carbide or carbonates such as calcite and magnesite, respectively, in C-enriched planetary interiors. The minimum amount of carbon needed for carbon saturation in the type of C-enriched rocky exoplanets considered in this study is 0.05–0.7 wt% (molar C/O ~ 0.002–0.03), which lies between the upper bounds of 200 ppm and 9 wt% for mantle-only and core-only planets, respectively.

Any amount of carbon exceeding the carbon-saturation limit would be in the form of graphite. If the graphite layer is deep enough to exceed pressures of 2–15 GPa, depending on the temperature profile, a diamond layer would exist beneath the graphite layer. Carbon in the form of graphite can significantly affect the mass of an exoplanet for a fixed radius. For example, only a 10 wt% graphite crust is sufficient to decrease the derived mass of Kepler-37b by 7%, a difference detectable by future space missions focusing on determinations of both mass and radius of rocky exoplanets

with insignificant gaseous envelopes. Rocky exoplanets with graphite-rich surfaces would appear dark in future observations because of low albedos due to graphite. Atmospheres of such planets are likely thin or nonexistent, and the detection of CO/CO_2 or CH_4 on its own cannot confirm the presence or absence of a graphite-rich surface. Surfaces of such planets are less likely to be hospitable for life because of the lack of life-bearing elements other than carbon.

Acknowledgments

Author Disclosure Statement

No competing financial interests exist.

References

Anderson, D.E., Bergin, E.A., Blake, G.A., Ciesla, F.J., Visser, R., and Lee, J.-E. (2017) Destruction of refractory carbon in protoplanetary disks. *Astrophys J* 845:13.

Armstrong, J.T. (1995) CITZAF: a package of correction programs for the quantitative electron microbeam X-ray analysis of thick polished materials, thin films, and particles. *Microbeam Anal* 4:177–200.

Batalha, N.M. (2014) Exploring exoplanet populations with NASA's Kepler Mission. *Proc Natl Acad Sci U S A* 111: 12647–12654.

Birch, F. (1947) Finite elastic strain of cubic crystals. *Phys Rev* 71:809–824.

Bizzarro, M., Baker, J.A., Haack, H., and Lundgaard, K.L. (2005) Rapid timescales for accretion and melting of differentiated planetesimals inferred from ^{26}Al-^{26}Mg chronometry. *Astrophys J Lett* 632:L41–L44.

Bond, J.C., O'Brien, D.P., and Lauretta, D.S. (2010) The compositional diversity of extrasolar terrestrial planets. I. In situ simulations. *Astrophys J* 715:1050–1070.

Boujibar, A., Andrault, D., Bouhifd, M.A., Bolfan-Casanova, N., Devidal, J.-L., and Trcera, N. (2014) Metal–silicate partitioning of sulphur, new experimental and thermodynamic constraints on planetary accretion. *Earth Planet Sci Lett* 391: 42–54.

Brewer, J.M., Fischer, D.A., Valenti, J.A., and Piskunov, N. (2016) Spectral properties of cool stars: extended abundance analysis of 1,617 planet-search stars. *Astrophys J Suppl Ser* 225:32.

Carter-Bond, J.C., O'Brien, D.P., Delgado Mena, E., Israelian, G., Santos, N.C., and González Hernández, J.I. (2012a) Low Mg/Si planetary host stars and their Mg-depleted terrestrial planets. *Astrophys J Lett* 747, L2.

Carter-Bond, J.C., O'Brien, D.P., and Raymond, S.N. (2012b) The compositional diversity of extrasolar terrestrial planets. II. Migration simulations. *Astrophys J* 760, 44.

Chi, H., Dasgupta, R., Duncan, M.S., and Shimizu, N. (2014) Partitioning of carbon between Fe-rich alloy melt and silicate melt in a magma ocean—implications for the abundance and origin of volatiles in Earth, Mars, and the Moon. *Geochim Cosmochim Acta* 139:447–471.

Colonna, F., Fasolino, A., and Meijer, E. (2011) High-pressure high-temperature equation of state of graphite from Monte Carlo simulations. *Carbon* 49:364–368.

Corgne, A., Wood, B.J., and Fei, Y. (2008) C- and S-rich molten alloy immiscibility and core formation of planetesimals. *Geochim Cosmochim Acta* 72:2409–2416.

Dasgupta, R. (2013) Ingassing, storage, and outgassing of terrestrial carbon through geologic time. *Rev Mineral Geochem* 75:183–229.

Dasgupta, R. and Walker, D. (2008) Carbon solubility in core melts in a shallow magma ocean environment and distribution of carbon between the Earth's core and the mantle. *Geochim Cosmochim Acta* 72:4627–4641.

Dasgupta, R., Buono, A., Whelan, G., and Walker, D. (2009) High-pressure melting relations in Fe-C-S systems: implications for formation, evolution, and structure of metallic cores in planetary bodies. *Geochim Cosmochim Acta* 73:6678–6691.

Dasgupta, R., Chi, H., Shimizu, N., Buono, A.S., and Walker, D. (2013) Carbon solution and partitioning between metallic and silicate melts in a shallow magma ocean: implications for the origin and distribution of terrestrial carbon. *Geochim Cosmochim Acta* 102:191–212.

Delgado Mena, E., Israelian, G., González Hernández, J.I., Bond, J.C., Santos, N.C., Udry, S., and Mayor, M. (2010) Chemical clues on the formation of planetary systems: C/O versus Mg/Si for HARPS GTO sample. *Astrophys J* 725:2349–2358.

Deng, L., Fei, Y., Liu, X., Gong, Z., and Shahar, A. (2013) Effect of carbon, sulfur and silicon on iron melting at high pressure: implications for composition and evolution of the planetary terrestrial cores. *Geochim Cosmochim Acta* 114:220–233.

Dorn, C., Khan, A., Heng, K., Connolly, J.A.D., Alibert, Y., Benz, W., and Tackley, P. (2015) Can we constrain the interior structure of rocky exoplanets from mass and radius measurements? *Astron Astrophys* 577:A83.

Duncan, M.S., Dasgupta, R., and Tsuno, K. (2017) Experimental determination of CO_2 content at graphite saturation along a natural basalt-peridotite melt join: implications for the fate of carbon in terrestrial magma oceans. *Earth Planet Sci Lett* 466:115–128.

Elkins-Tanton, L.T. (2012) Magma oceans in the inner solar system. *Ann Rev Earth Planet Sci* 40:113–139.

Fei, Y., Murphy, C., Shibazaki, Y., Shahar, A., and Huang, H. (2016) Thermal equation of state of hcp-iron: constraint on the density deficit of earth's solid inner core. *Geophys Res Lett* 43:6837–6843. 2016GL069456.

Fortier, A., Beck, T., Benz, W., Broeg, C., Cessa, V., Ehrenreich, D., and Thomas, N. (2014) CHEOPS: a space telescope for ultra-high precision photometry of exoplanet transits. In *Space Telescopes and Instrumentation 2014: Optical, Infrared, and Millimeter Wave*, Proc SPIE 91432J (28 August 2014).

Ghiringhelli, L.M., Los, J.H., Meijer, E.J., Fasolino, A., and Frenkel, D. (2005) Modeling the phase diagram of carbon. *Phys Rev Lett* 94:145701.

Giordano, D., Russell, J.K., and Dingwell, D.B. (2008) Viscosity of magmatic liquids: a model. *Earth Planet Sci Lett* 271:123–134.

Hakim, K., Rivoldini, A., Van Hoolst, T., Cottenier, S., Jaeken, J., Chust, T., and Steinle-Neumann, G. (2018a) A new ab initio equation of state of hcp-Fe and its implication on the interior structure and mass-radius relations of rocky super-Earths. *Icarus* 313:61–78.

Hakim, K., van Westrenen, W., and Dominik, C. (2018b) Capturing the oxidation of silicon carbide in rocky exoplanetary interiors. *Astron Astrophys* 618:L6.

Hashizume, K. and Sugiura, N. (1998) Transportation of gaseous elements and isotopes in a thermally evolving chondritic planetesimal. *Meteorit Planet Sci* 33:1181–1195.

Hevey, P.J. and Sanders, I.S. (2006) A model for planetesimal meltdown by [26]Al and its implications for meteorite parent bodies. *Meteorit Planet Sci* 41:95–106.

Hirose, K. and Fei, Y. (2002) Subsolidus and melting phase relations of basaltic composition in the uppermost lower mantle. *Geochim Cosmochim Acta* 66:2099–2108.

Holzheid, A., Palme, H., and Chakraborty, S. (1997) The activities of NiO, CoO and FeO in silicate melts. *Chem Geol* 139:21–38.

Javoy, M., Kaminski, E., Guyot, F., Andrault, D., Sanloup, C., Moreira, M., Labrosse, S., Jambon, A., Agrinier, P., Davaille, A., and Jaupart, C. (2010) The chemical composition of the Earth: enstatite chondrite models. *Earth Planet Sci Lett* 293:259–268.

Johansen, A., Oishi, J.S., Mac Low, M.-M., Klahr, H., Henning, T., and Youdin, A. (2007) Rapid planetesimal formation in turbulent circumstellar disks. *Nature* 448:1022–1025.

Jugo, P.J., Luth, R.W., and Richards, J.P. (2005) Experimental data on the speciation of sulfur as a function of oxygen fugacity in basaltic melts. *Geochim Cosmochim Acta* 69:497–503.

Jugo, P.J., Wilke, M., and Botcharnikov, R.E. (2010) Sulfur K-edge XANES analysis of natural and synthetic basaltic glasses: implications for S speciation and S content as function of oxygen fugacity. *Geochim Cosmochim Acta* 74:5926–5938.

Klarmann, L., Ormel, C.W., and Dominik, C. (2018) Radial and vertical dust transport inhibit refractory carbon depletion in protoplanetary disks. *Astron Astrophys* 618, L1.

Kruijer, T.S., Fischer-Godde, M., Kleine, T., Sprung, P., Leya, I., and Wieler, R. (2013) Neutron capture on Pt isotopes in iron meteorites and the Hf-W chronology of core formation in planetesimals. *Earth Planet Sci Lett* 361:162–172.

Kuchner, M.J. and Seager, S. (2005) Extrasolar carbon planets. ArXiv *Astrophysics* e-prints.

Kushiro, I. and Walter, M.J. (1998) Mg-Fe partitioning between olivine and mafic-ultramafic melts. *Geophys Res Lett* 25:2337–2340.

Lazar, C., Zhang, C., Manning, C.E., and Mysen, B.O. (2014) Redox effects on calcite-portlandite-fluid equilibria at forearc conditions: carbon mobility, methanogenesis, and reduction melting of calcite. *Am Mineral* 99:1604–1615.

Lee, J. and Morita, K. (2002) Evaluation of surface tension and adsorption for liquid Fe-S alloys. *ISIJ Int* 42:588–594.

Lee, J.-E., Bergin, E.A., and Nomura, H. (2010) The solar nebula on fire: a solution to the carbon deficit in the inner solar system. *Astrophys J Lett* 710, L21.

Léger, A., Rouan, D., Schneider, J., Barge, P., Fridlund, M., Samuel, B., Ollivier, M., Guenther, E., Deleuil, M., Deeg, H.J., Auvergne, M., Alonso, R., Aigrain, S., Alapini, A.,

Almenara, J.M., Baglin, A., Barbieri, M., Bruntt, H., Borde, P., Bouchy, F., Cabrera, J., Catala, C., Carone, L., Carpano, S., Csizmadia, S., Dvorak, R., Erikson, A., Ferraz-Mello, S., Foing, B., Fressin, F., Gandolfi, D., Gillon, M., Gondoin, P., Grasset, O., Guillot, T., Hatzes, A., Hebrard, G., Jorda, L., Lammer, H., Llebaria, A., Loeillet, B., Mayor, M., Mazeh, T., Moutou, C., Paetzold, M., Pont, F., Queloz, D., Rauer, H., Renner, S., Samadi, R., Shporer, A., Sotin, C., Tingley, B., Wuchterl, G., *et al.* (2009) Transiting exoplanets from the CoRoT space mission. VIII. CoRoT-7b: the first super-Earth with measured radius. *Astron Astrophys* 506:287–302.

Li, Y., Dasgupta, R., and Tsuno, K. (2015) The effects of sulfur, silicon, water, and oxygen fugacity on carbon solubility and partitioning in Fe-rich alloy and silicate melt systems at 3 GPa and 1600°C: implications for core-mantle differentiation and degassing of magma oceans and reduced planetary mantles. *Earth Planet Sci Lett* 415:54–66.

Li, Y., Dasgupta, R., Tsuno, K., Monteleone, B., and Shimizu, N. (2016) Carbon and sulfur budget of the silicate Earth explained by accretion of differentiated planetary embryos. *Nat Geosci* 9:781–785.

Lord, O.T., Walter, M.J., Dasgupta, R., Walker, D., and Clark, S.M. (2009) Melting in the Fe-C system to 70 GPa. *Earth Planet Sci Lett* 284:157–167.

Madhusudhan, N., Lee, K.K.M., and Mousis, O. (2012) A possible carbon-rich interior in super-Earth 55 Cancri e. *Astrophys J Lett* 759:L40.

Marty, B., Alexander, C.M.O., and Raymond, S.N. (2013) Primordial origins of Earth's carbon. *Rev Mineral Geochem* 75:149–181.

McDade, P., Wood, B.J., van Westrenen, W., Brooker, R., Gudmundsson, G., Soulard, H., Najorka, J., and Blundy, J. (2002) Pressure corrections for a selection of piston-cylinder cell assemblies. *Mineral Mag* 66:1021–1028.

Morard, G. and Katsura, T. (2010) Pressure–temperature cartography of Fe–S–Si immiscible system. *Geochim Cosmochim Acta* 74:3659–3667.

Moriarty, J., Madhusudhan, N., and Fischer, D. (2014) Chemistry in an evolving protoplanetary disk: effects on terrestrial planet composition. *Astrophys J* 787:81.

Nabiei, F., Badro, J., Dennenwaldt, T., Oveisi, E., Cantoni, M., Hébert, C., El Goresy, A., Barrat, J.-A., and Gillet P. (2018) A large planetary body inferred from diamond inclusions in a ureilite meteorite. *Nat Commun* 9:1327.

Nakajima, T. and Sorahana, S. (2016) Carbon-to-oxygen ratios in M dwarfs and solar-type stars. *Astrophys J* 830:159.

Nisr, C., Meng, Y., MacDowell, A.A., Yan, J., Prakapenka, V., and Shim, S.-H. (2017) Thermal expansion of SiC at high pressure-temperature and implications for thermal convection in the deep interiors of carbide exoplanets. *J Geophys Res Planets* 122:124–133.

O'Neill, H.S.C. and Eggins, S.M. (2002) The effect of melt composition on trace element partitioning: an experimental investigation of the activity coefficients of FeO, NiO, CoO, MoO_2 and MoO_3 in silicate melts. *Chem Geol* 186:151–181.

Peplowski, P.N., Klima, R.L., Lawrence, D.J., Ernst, C.M., Denevi, B.W., Frank, E.A., Goldsten, J.O., Murchie, S.L., Nittler, L.R., and Solomon, S.C. (2016) Remote sensing evidence for an ancient carbon-bearing crust on Mercury. *Nat Geosci* 9:273–276.

Petigura, E.A. and Marcy, G.W. (2011) Carbon and oxygen in nearby stars: keys to protoplanetary disk chemistry. *Astrophys J* 735:41.

Ragazzoni, R., Magrin, D., Rauer, H., Pagano, I., Nascimbeni, V., Piotto, G., Piazza, D., Levacher, P., Schweitzer, M., Basso, S., Bandy, T., Benz, W., Bergomi, M., Biondi, F., Boerner, A., Borsa, F., Brandeker, A., Brändli, M., Bruno, G., Cabrera, J., Chinellato, S., De Roche, T., Dima, M., Erikson, A., Farinato, J., Munari, M., Ghigo, M., Greggio, D., Gullieuszik, M., Klebor, M., Marafatto, L., Mogulsky, V., Peter, G., Rieder, M., Sicilia, D., Spiga, D., Viotto, V., Wieser, M., Heras, A.M., Gondoin, P., Bodin, P., and Catala, C. (2016) PLATO: a multiple telescope spacecraft for exoplanets hunting. In *Space Telescopes and Instrumentation 2016: Optical, Infrared, and Millimeter Wave*, Proc SPIE 990428 (29 July 2016).

Rai, N. and van Westrenen, W. (2013) Core-mantle differentiation in Mars. *J Geophys Res (Planets)* 118:1195–1203.

Ricker, G.R., Winn, J.N., Vanderspek, R., Latham, D.W., Bakos, G.Á., Bean, J.L., Berta-Thompson, Z.K., Brown, T.M., Buchhave, L., Butler, N.R., Butler, R.P., Chaplin, W.J., Charbonneau, D., Christensen-Dalsgaard, J., Clampin, M., Deming, D., Doty, J., De Lee, N., Dressing, C., Dunham, E.W., Endl, M., Fressin, F., Ge, J., Henning, T., Holman, M.J., Howard, A.W., Ida, S., Jenkins, J., Jernigan, G., Johnson, J.A., Kaltenegger, L., Kawai, N., Kjeldsen, H., Laughlin, G., Levine, A.M., Lin, D., Lissauer, J.J., MacQueen, P., Marcy, G., McCullough, P.R., Morton, T.D., Narita, N., Paegert, M., Palle, E., Pepe, F., Pepper, J., Quirrenbach, A., Rinehart, S.A., Sasselov, D., Sato, B., Seager, S., Sozzetti, A., Stassun, K.G., Sullivan, P., Szentgyorgyi, A., Torres, G., Udry, S., and Villasenor, J. (2014) The Transiting Exoplanet Survey Satellite (TESS). In *Space Telescopes and Instrumentation 2014: Optical, Infrared, and Millimeter Wave*, Proc SPIE 914320 (22–27 June 2014).

Rohrbach, A., Ghosh, S., Schmidt, M.W., Wijbrans, C.H., and Klemme, S. (2014) The stability of Fe-Ni carbides in the Earth#700s mantle: evidence for a low Fe-Ni-C melt fraction in the deep mantle. *Earth Planet Sci Lett* 388:211–221.

Rohrbach, A. and Schmidt, M.W. (2011) Redox freezing and melting in the Earth's deep mantle resulting from carbon-iron redox coupling. *Nature* 472:209–212.

Santos, N.C., Adibekyan, V., Dorn, C., Mordasini, C., Noack, L., Barros, S.C.C., Delgado-Mena, E., Demangeon, O., Faria, J.P., Israelian, G., and Sousa, S.G. (2017) Constraining planet structure and composition from stellar chemistry: trends in different stellar populations. *Astron Astrophys* 608: A94.

Sata, N., Hirose, K., Shen, G., Nakajima, Y., Ohishi, Y., and Hirao, N. (2010) Compression of FeSi, Fe_3C, $Fe_{0.95}O$, and FeS under the core pressures and implication for light element in the Earth's core. *J Geophys Res Solid Earth* 115, B09204.

Schäfer, U., Yang, C.-C., and Johansen, A. (2017) Initial mass function of planetesimals formed by the streaming instability. *Astron Astrophys* 597, A69.

Seager, S., Kuchner, M., Hier-Majumder, C.A., and Militzer, B. (2007) Mass-radius relationships for solid exoplanets. *Astrophys J* 669:1279–1297.

Shabalin, I.L. (2014) Carbon (graphene/graphite). In *Ultra-high temperature materials I*. 7–235. Springer, Dordrecht, Netherlands.

Smythe, D.J., Wood, B.J., and Kiseeva, E.S. (2017) The S content of silicate melts at sulfide saturation: new experiments and a model incorporating the effects of sulfide composition. *Am Mineral* 102:795–803.

Southworth, J., Mancini, L., Madhusudhan, N., Mollière, P., Ciceri, S., and Henning, T. (2017) Detection of the atmosphere of the 1.6M exoplanet GJ1132 b. *Astron J* 153:191.

Stassun, K.G., Collins, K.A., and Gaudi, B.S. (2017) Accurate empirical radii and masses of planets and their host stars with Gaia parallaxes. *Astron J* 153:136.

Steenstra, E.S., Knibbe, J.S., Rai, N., and van Westrenen, W. (2016) Constraints on core formation in Vesta from metal-silicate partitioning of siderophile elements. *Geochim Cosmochim Acta* 177:48–61.

Stewart, A.J., Schmidt, M.W., van Westrenen, W., and Liebske, C. (2007) Mars: a new core-crystallization regime. *Science* 316:1323.

Stixrude, L. and Lithgow-Bertelloni, C. (2005) Thermodynamics of mantle minerals—I. Physical properties. *Geophys J Int* 162:610–632.

Takahashi, S., Ohtani, E., Terasaki, H., Ito, Y., Shibazaki, Y., Ishii, M., Funakoshi, K.-I., and Higo, Y. (2013) Phase relations in the carbon-saturated C-Mg-Fe-Si-O system and C and Si solubility in liquid Fe at high pressure and temperature: implications for planetary interiors. *Phys Chem Miner* 40: 647–657.

Thiabaud, A., Marboeuf, U., Alibert, Y., Leya, I., and Mezger, K. (2015) Elemental ratios in stars vs planets (Research Note). *Astron Astrophys* 580, A30.

Toplis, M.J. (2005) The thermodynamics of iron and magnesium partitioning between olivine and liquid: criteria for assessing and predicting equilibrium in natural and experimental systems. *Contrib Mineral Petrol* 149:22–39.

Tsuno, K. and Dasgupta, R. (2015) Fe-Ni-Cu-C-S phase relations at high pressures and temperatures—The role of sulfur in carbon storage and diamond stability at mid-to deep-upper mantle. *Earth Planet Sci Lett* 412:132–142.

Tsuno, K., Ohtani, E., and Terasaki, H. (2007) Immiscible two-liquid regions in the Fe–O–S system at high pressure: implications for planetary cores. *Phys Earth Planet Inter* 160: 75–85.

Unterborn, C.T., Kabbes, J.E., Pigott, J.S., Reaman, D.M., and Panero, W.R. (2014) The role of carbon in extrasolar planetary geodynamics and habitability. *Astrophys J* 793: 124.

Unterborn, C.T., Dismukes, E.E., and Panero, W.R. (2016) Scaling the Earth: a sensitivity analysis of terrestrial exoplanetary interior models. *Astrophys J* 819:32.

Valencia, D., O'Connell, R.J., and Sasselov, D. (2006) Internal structure of massive terrestrial planets. *Icarus* 181:545–554.

Valencia, D., O'Connell, R.J., and Sasselov, D.D. (2009) The role of high-pressure experiments on determining super-Earth properties. *Astrophys Space Sci* 322:135–139.

Valencia, D., Sasselov, D.D., and O'Connell, R.J. (2007) Radius and structure models of the first super-Earth planet. *Astrophys J* 656:545–551.

van Kan Parker, M., Mason, P. R.D., and van Westrenen, W. (2011) Trace element partitioning between ilmenite, armalcolite and anhydrous silicate melt: implications for the formation of lunar high-Ti mare basalts. *Geochim Cosmochim Acta* 75:4179–4193.

Wagner, F.W., Sohl, F., Hussmann, H., Grott, M., and Rauer, H. (2011) Interior structure models of solid exoplanets using material laws in the infinite pressure limit. *Icarus* 214:366–376.

Wang, C., Hirama, J., Nagasaka, T., and Ban-Ya., S. (1991) Phase equilibria of liquid Fe-S-C ternary system. *ISIJ Int* 31: 1292–1299.

Watson, E.B., Wark, D.A., Price, J.D., and Van Orman, J.A. (2002) Mapping the thermal structure of solid-media pressure assemblies. *Contrib Mineral Petrol* 142:640–652.

Whitehouse, L.J., Farihi, J., Green, P.J., Wilson, T.G., and Subasavage, J.P. (2018) Dwarf carbon stars are likely metal-poor binaries and unlikely hosts to carbon planets. *Mon Not Roy Astron Soc*, 479:3873–3878.

Address correspondence to:
Kaustubh Hakim
Center for Space and Habitability
University of Bern
3012 Bern
*Switzerland*

E-mail: hakim.kaustubh@gmail.com

Abbreviations Used

EC = equilibrium chemistry
EPMA = Electron Probe Micro-Analyzer
FCMAS+CSO = Fe-Ca-Mg-Al-Si-C-S-O
FMS+CO = Fe-Mg-Si-C-O
IW = iron-wüstite
SC = sequential condensation chemistry
TC = third bulk composition based on equilibrium chemistry
WDS = wavelength dispersive spectroscopy

Appendix 1. Experimental Sample Assembly

Sample powder was inserted in a 1.6-mm-wide graphite capsule with a graphite lid (Appendix Fig. A1). This graphite capsule was put into a 2-mm-wide Pt capsule that was sealed and arc-welded on both ends with a Lampert PUK 3 welder. The Pt capsule was placed in an MgO rod sealed with MgO cement. The MgO rod was introduced in a graphite furnace, thermally insulated by surrounding it with an inner Pyrex sleeve and an outer talc sleeve. A four-bore Al_2O_3 rod, through which thermocouple wires were threaded, was placed on top of the MgO rod. Pressure calibration of the assembly was performed by bracketing the albite to jadeite plus quartz and fayalite to ferrosilite plus quartz transitions (van Kan Parker *et al.*, 2011). The resulting pressure correction of 3% is consistent with literature data (McDade *et al.*, 2002). On top of the talc/Pyrex assembly, a hardened silver steel plug with a pyrophyllite ring and a hole for thermocouple was placed. A $W_{97}Re_3/W_{75}Re_{25}$ (type D) thermocouple was placed in the thermocouple hole directly above the Pt capsule. The distance of 1–3.5 mm between the thermocouple tip and the sample produced a temperature difference of 10 K (Watson *et al.*, 2002).
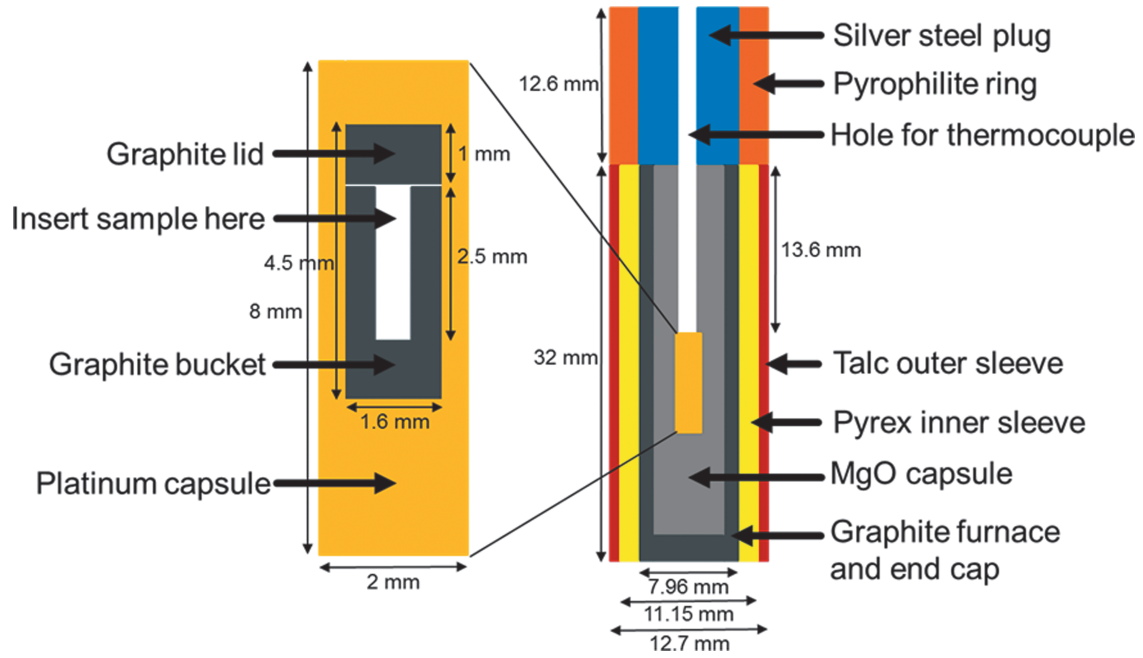
APPENDIX FIG. A1. Components of the sample assembly used to perform high-pressure experiments.

Appendix 2. Oxygen Fugacity Calculations

We computed oxygen fugacity (f_{O_2}) in our experiments with respect to the iron-wüstite (IW) buffer using the following equation:

$$\log f_{O_2}(\Delta\text{IW}) = 2\log\frac{X^{\text{sil}}_{\text{FeO}}\gamma^{\text{sil}}_{\text{FeO}}}{X^{\text{alloy}}_{\text{Fe}}\gamma^{\text{alloy}}_{\text{Fe}}},$$

where $X^{\text{sil}}_{\text{FeO}}$ and $\gamma^{\text{sil}}_{\text{FeO}}$ are the mole fraction and the activity of FeO in silicate melt, and $X^{\text{alloy}}_{\text{Fe}}$ and $\gamma^{\text{alloy}}_{\text{Fe}}$ are the mole fraction and the activity of Fe in S-rich Fe alloy. We assumed a non-ideal solution behavior of silicate melt and iron alloy, which implies nonunity values for $\gamma^{\text{sil}}_{\text{FeO}}$ and $\gamma^{\text{alloy}}_{\text{Fe}}$. A fixed value of $\gamma^{\text{sil}}_{\text{FeO}} \sim 1.5$ and the average from the two studies that deter-

mined $\gamma^{\text{sil}}_{\text{FeO}}$ for a wide range of melt compositions were used (Holzheid *et al.*, 1997; O'Neill and Eggins, 2002), assuming no significant pressure effect on silFeO (Toplis, 2005). We computed $\gamma^{\text{alloy}}_{\text{Fe}}$ from Lee and Morita (2002) using

$$\ln\gamma^{\text{alloy}}_{\text{Fe}} = \frac{\alpha_2}{2}\left(1-X^{\text{alloy}}_{\text{Fe}}\right)^2 + \frac{\alpha_3}{3}\left(1-X^{\text{alloy}}_{\text{Fe}}\right)^3 + \frac{\alpha_4}{4}\left(1-X^{\text{alloy}}_{\text{Fe}}\right)^4,$$

where $\alpha_2 = 3.80$, $\alpha_3 = -5.24$, and $\alpha_4 = 2.58$ at 1623 K, $\alpha_2 = 4.01$, $\alpha_3 = -5.52$, and $\alpha_4 = 2.71$ at 1723 K, and $\alpha_2 = 4.25$, $\alpha_3 = -5.84$, and $\alpha_4 = 2.87$ at 1823 K. In the ab-

sence of silicate melts, as in some of our experiments, we used X_{FeO} of olivine instead. Our oxygen fugacity calculations are given in Table 2.

Appendix 3. Mineral/Melt Equilibrium

To assess mineral/melt equilibrium, we calculated olivine/melt and orthopyroxene/melt Fe-Mg exchange coefficients, K_D and K'_D, following Kushiro and Walter (1998) and Toplis (2005), respectively,

$$K_{D_{\text{Olv}-\text{Melt}}}^{\text{Mg}-\text{Fe}} = \frac{X^{\text{Mg}}_{\text{Melt}}/X^{\text{Mg}}_{\text{Olv}}}{X^{\text{Fe}}_{\text{Melt}}/X^{\text{Fe}}_{\text{Olv}}},$$

$$K'^{\text{Mg}-\text{Fe}}_{D_{\text{Olv}-\text{Melt}}} = \exp\left[\left(\frac{-6766}{RT}-\frac{7.34}{R}\right)+\ln\left[0.036X^{\text{SiO}_2}_{\text{Melt}}-0.22\right]+\left(\frac{3000\left(1-2Y^{\text{Mg}/(\text{Mg}+\text{Fe})}_{\text{Olv}}\right)}{RT}\right)+\left(\frac{0.035(P-1)}{RT}\right)\right],$$

where X^a_b is mol% of a in b, $Y^{\text{Mg}/(\text{Mg}+\text{Fe})}_{\text{Olv}}$ is molar Mg/(Mg+Fe) in olivine, R is the gas constant, T is temperature in K, and P is pressure in bar. Our calculations of K_D and K'_D for all runs result in values between $0.22-0.38$ and $0.24-0.28$, respectively (Table 3). According to Toplis (2005), this range is consistent with equilibrium. For orthopyroxene in the TC run at 2 GPa and 1823 K, and the EC runs at 1 GPa and 1723 K and 2 GPa and 1823 K, K_D ranges between 0.21 and 0.32, also within the acceptable range for equilibrated systems.

Appendix References

van Kan Parker, M., Mason, P. R.D., and van Westrenen, W. (2011) Trace element partitioning between ilmenite, armalcolite and anhydrous silicate melt: implications for the formation of lunar high-Ti mare basalts. *Geochim Cosmochim Acta* 75:4179–4193.

McDade, P., Wood, B.J., Van Westrenen, W., Brooker, R., Gudmundsson, G., Soulard, H., Najorka, J., and Blundy, J. (2002) Pressure corrections for a selection of piston-cylinder cell assemblies. *Mineral Mag* 66:1021–1028.

Watson, E.B., Wark, D.A., Price, J.D., and Van Orman, J.A. (2002) Mapping the thermal structure of solid-media pressure assemblies. *Contrib Mineral Petrol* 142:640–652.

Holzheid, A., Palme, H., and Chakraborty, S. (1997) The activities of NiO, CoO and FeO in silicate melts. *Chem Geol* 139:21–38.

O'Neill, H.S.C., and Eggins, S.M. (2002) The effect of melt composition on trace element partitioning: an experimental investigation of the activity coefficients of FeO, NiO, CoO, MoO$_2$ and MoO$_3$ in silicate melts. *Chem Geol* 186:151–181.

Toplis, M.J. (2005) The thermodynamics of iron and magnesium partitioning between olivine and liquid: criteria for assessing and predicting equilibrium in natural and experimental systems. *Contrib Mineral Petrol* 149: 22–39.

Lee, J. and Morita, K. (2002) Evaluation of surface tension and adsorption for liquid Fe-S alloys. *ISIJ Int* 42:588–594.

Kushiro, I. and Walter, M.J. (1998) Mg-Fe partitioning between olivine and mafic-ultramafic melts. *Geophys Res Lett* 25: 2337–2340.